



Hot planets around cool stars - two short-period mini-Neptunes transiting the late K-dwarf TOI-1260

Downloaded from: <https://research.chalmers.se>, 2024-04-19 20:20 UTC

Citation for the original published paper (version of record):

Georgieva, I., Persson, C., Barragan, O. et al (2021). Hot planets around cool stars - two short-period mini-Neptunes transiting the late K-dwarf TOI-1260. Monthly Notices of the Royal Astronomical Society, 505(4): 4684-4701.
<http://dx.doi.org/10.1093/mnras/stab1464>

N.B. When citing this work, cite the original published paper.



Hot planets around cool stars – two short-period mini-Neptunes transiting the late K-dwarf TOI-1260

I. Y. Georgieva,^{1★} C. M. Persson,¹ O. Barragán,² G. Nowak,^{3,4} M. Fridlund,⁵ D. Locci,⁶ E. Palle,^{3,4} R. Luque,^{3,4} I. Carleo,⁷ D. Gandolfi,⁸ S. R. Kane,⁹ J. Korth,¹⁰ K. G. Stassun,¹¹ J. Livingston,¹² E. C. Matthews,^{13,14} K. A. Collins,¹⁵ S. B. Howell,¹⁶ L. M. Serrano,⁸ S. Albrecht,^{17,18} A. Bieryla,¹⁵ C. E. Brasseur,¹⁹ D. Ciardi,²⁰ W. D. Cochran,²¹ K. D. Colon,²² I. J. M. Crossfield,²³ Sz. Csizmadia,²⁴ H. J. Deeg,^{3,4} M. Esposito,²⁵ E. Furlan,²⁶ T. Gan,²⁷ E. Goffo,⁸ E. Gonzales,²⁸ S. Grziwa,²⁹ E. W. Guenther,²⁵ P. Guerra,³⁰ T. Hirano,^{31,32} J. M. Jenkins,¹⁶ E. L. N. Jensen,³³ P. Kabáth,³⁴ E. Knudstrup,^{17,18} K. W. F. Lam,³⁵ D. W. Latham,¹⁵ A. M. Levine,¹³ R. A. Matson,³⁶ S. McDermott,³⁷ H. L. M. Osborne,³⁸ M. Paegert,¹⁵ S. N. Quinn,¹⁵ S. Redfield,⁷ G. R. Ricker,¹³ J. E. Schlieder,³⁹ N. J. Scott,¹⁶ S. Seager,^{13,40,41} A. M. S. Smith,²⁴ P. Tenenbaum,^{16,42} J. D. Twicken,^{16,42} R. Vanderspek,¹³ V. Van Eylen³⁸ and J. N. Winn⁴³

Affiliations are listed at the end of the paper

Accepted 2021 May 15. Received 2021 May 6; in original form 2020 December 18

ABSTRACT

We present the discovery and characterization of two sub-Neptunes in close orbits, as well as a tentative outer planet of a similar size, orbiting TOI-1260 – a low metallicity K6 V dwarf star. Photometry from *Transiting Exoplanet Survey Satellite* (*TESS*) yields radii of $R_b = 2.33 \pm 0.10$ and $R_c = 2.82 \pm 0.15 R_\oplus$, and periods of 3.13 and 7.49 d for TOI-1260 b and TOI-1260 c, respectively. We combined the *TESS* data with a series of ground-based follow-up observations to characterize the planetary system. From HARPS-N high-precision radial velocities we obtain $M_b = 8.6^{+1.4}_{-1.5}$ and $M_c = 11.8^{+3.4}_{-3.2} M_\oplus$. The star is moderately active with a complex activity pattern, which necessitated the use of Gaussian process regression for both the light-curve detrending and the radial velocity modelling, in the latter case guided by suitable activity indicators. We successfully disentangle the stellar-induced signal from the planetary signals, underlining the importance and usefulness of the Gaussian process approach. We test the system's stability against atmospheric photoevaporation and find that the TOI-1260 planets are classic examples of the structure and composition ambiguity typical for the 2–3 R_\oplus range.

Key words: techniques: photometric – techniques: radial velocities – planets and satellites: atmospheres – planets and satellites: individual: TOI-1260b, c – planets and satellites: composition – stars: low-mass – planetary systems.

1 INTRODUCTION

Thanks to space-based photometry from missions like *Convection, Rotation and planetary Transits* (CoRoT; Baglin et al. 2006), Kepler and K2 (Borucki et al. 2010; Howell et al. 2014) and *Transiting Exoplanet Survey Satellite* (*TESS*; Ricker et al. 2015), the detection of shallow transits caused by small planets ($\lesssim 4 R_\oplus$) around faint stars has been made possible. The current exoplanet census shows that the most commonly detected population of planets is well represented by the so-called sub-Neptunes ($2 \lesssim R_\oplus \lesssim 4$) and rocky super-Earths ($1 \lesssim R_\oplus \lesssim 1.5$), with the radius valley (Lopez & Fortney 2013; Owen & Wu 2013; Fulton et al. 2017; Van Eylen et al. 2018, 2021), characterized by a paucity of planets between 1.5 and 2 R_\oplus (Fulton et al. 2017). This range has been shown to shift to smaller radii for low-mass stars (Fulton & Petigura 2018; Wu 2019; Cloutier & Menou 2020; Van Eylen et al. 2021). An interesting observation

about this population is the apparent ambiguity of the members' structures and compositions. Valencia, Sasselo & O'Connell (2007) first discussed the continuous wide range of planet compositions for a given mass and radius, while discrete reference planet models by Zeng, Sasselo & Jacobsen (2016) and Zeng et al. (2019) show possible combinations of a rocky core with a H–He envelope, water-dominated worlds, as well as combinations of rock and ice bounded by H–He envelopes. This ambiguity is the result of the observed overlap between both the masses and radii of the two populations. Otegi, Bouchy & Helled (2020) report the transition range between sub-Neptunes to super-Earths to be 5–25 M_\oplus and 2–3 R_\oplus , which the TOI-1260 planets presented in this work comfortably fall in.

Moving towards solving the aforementioned composition ambiguity would require understanding the dependence of close-in ($P_{\text{orb}} < 10$ d) small (2–3 R_\oplus) planets on parameters like the stellar mass (Fulton & Petigura 2018), metallicity (Wilson et al. 2018; Dong et al. 2018; Wilson et al. 2018), age (Berger et al. 2020), high-energy irradiation (McDonald, Kreidberg & Lopez 2019a), as well as the

* E-mail: iskra.georgieva@chalmers.se

Table 1. Main identifiers, equatorial coordinates, proper motion, parallax, optical and infrared magnitudes, and fundamental parameters of TOI-1260.

Parameter	Value	Source
<i>Main identifiers</i>		
TIC 355867695		ExoFOP ^a
2MASSJ10283500 + 6551163		ExoFOP
UCAC4 780-023265		ExoFOP
WISE J102834.71 + 655115.5		ExoFOP
APASS 59325479		ExoFOP
<i>Equatorial coordinates, parallax, and proper motion</i>		
RA (J2000.0)	10 ^h 28 ^m 34 ^s .56	Gaia DR3 ^b
Dec. (J2000.0)	+65°51'15".07	Gaia DR3
π (mas)	13.6226 ± 0.0147	Gaia DR3
μ_α (mas yr ⁻¹)	-177.340 ± 0.012	Gaia DR3
μ_δ (mas yr ⁻¹)	-81.693 ± 0.013	Gaia DR3
<i>Optical and near-infrared photometry</i>		
TESS	10.812 ± 0.006	TIC v8 ^c
G	11.5655 ± 0.0028 ^d	Gaia DR3
B _p	12.2955 ± 0.0030 ^d	Gaia DR3
R _p	10.7415 ± 0.0038 ^d	Gaia DR3
B	13.259 ± 0.088	APASS
V	11.875 ± 0.165	APASS
g	12.702 ± 0.060	APASS
J	9.698 ± 0.023	2MASS
H	9.105 ± 0.027	2MASS
K _s	8.950 ± 0.022	2MASS
W1	8.891 ± 0.023	AllWISE
W2	8.964 ± 0.020	AllWISE
W3	8.880 ± 0.023	AllWISE
W4	9.215 ± 0.453	AllWISE

Notes.^a <https://exofop.ipac.caltech.edu/>

^b Gaia Collaboration et al. (2021).

^c Stassun et al. (2018b).

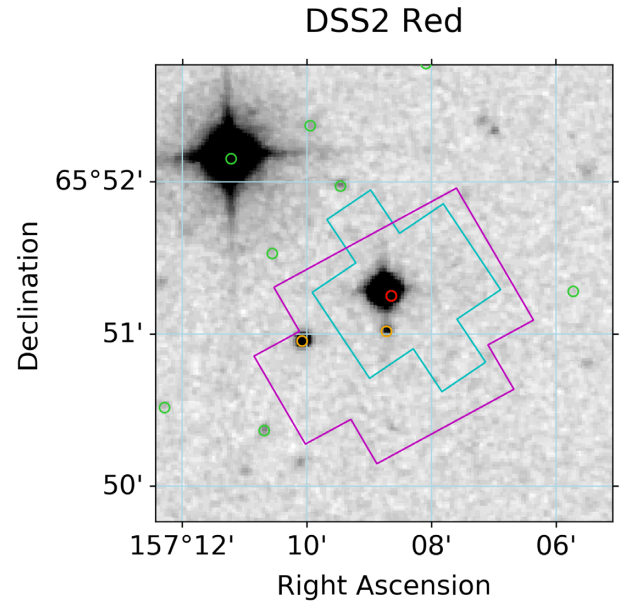
^dUncertainties from the VizieR Catalogue.

widely studied planetary mass, radius, period/semimajor axis. That said, while relatively precise radii are available from *TESS*, to place planets in the context of structure and composition models, we need precise mass estimates, and lots of them, as they are an indispensable piece of this puzzle.

The acquisition of precise masses is made possible thanks to high precision radial velocity (RV) measurements, performed by second-generation spectrographs, such as ESO's HARPS (Mayor et al. 2003) and HARPS-N (Cosentino et al. 2012), HIRES (Vogt et al. 1994), CARMENES (Quirrenbach et al. 2014, 2018), and more recently ESPRESSO (Pepe et al. 2010, 2021), EXPRES (Jurgenson et al. 2016) and more. Unfortunately, stellar activity can often be a complicating factor in obtaining accurate orbital solutions for the planet candidates. Great care and caution must be taken in accounting for this activity, the complexity of which may necessitate the use of more sophisticated methods than sinusoid fitting. This problem is further exacerbated the less massive and farther out from its star a planet is, as the precision required for a solid detection grows accordingly.

In this context, we present the discovery and characterization of the TOI-1260 system – a moderately active K6 V dwarf hosting two close-in ($P < 10$ d) transiting sub-Neptunes, as well as a tentative outer planet of similar size and an implied longer period.

The paper is organized as follows. Section 2 contains a summary of the space and ground-based observations of TOI-1260 as well as frequency analysis of the RVs and activity indicators, Section 3 describes the stellar modelling, and in Section 4 we present our joint

**Figure 1.** 3 arcmin × 3 arcmin DSS2 (red filter) image with the Sectors 14 and 21 SPOC photometric apertures outlined in cyan and magenta, respectively. Coloured circles denote the positions of *Gaia* DR2 sources within 2 arcmin of TOI-1260.

RV and transit analysis. In Section 5, we discuss our findings and results and we summarize our conclusions in Section 6.

2 OBSERVATIONS

Apart from space-based photometry from *TESS*, we obtained ground-based follow-up photometry from the Las Cumbres Observatory Global Telescope (LCOGT; Brown et al. 2013). We searched for stellar companions using Adaptive Optics (AO) and speckle imaging. To measure the planetary masses we observed TOI-1260 with HARPS-N.

2.1 TESS photometry

TESS first observed TOI-1260 in Sector 14 between 2019 July 18 and 2019 August 15 on camera 4, CCD 3, and again in Sector 21 from 2020 January 21 to 2020 February 18 on camera 2, CCD 2. The target identifiers, coordinates, proper motion, and magnitudes are listed in Table 1. Fig. 1 shows a 3 arcmin × 3 arcmin digitized sky survey 2 (DSS-2, red filter) image centred on TOI-1260, marked by the red circle. The orange circles inside the Science Processing Operations Center (SPOC; Jenkins et al. 2016) apertures of the two sectors are potentially contaminating sources (TIC 841176092 with $V_{\text{mag}} \approx 19$ and TIC 138477027 with $V_{\text{mag}} \approx 16.2$ at 13.9 and 40 arcsec away from TOI-1260, respectively). However, the difference image centroid analyses performed for both TOIs detected in the SPOC pipeline, together with the ground-based follow-up observations discussed in the following sections, exclude this from being the case. The SPOC pipeline (Twicken et al. 2010; Morris et al. 2017) uses Simple Aperture Photometry (SAP) to generate stellar light curves, where common instrumental systematics, including dilution, are removed via the Presearch Data Conditioning (PDCSAP) algorithm (Smith et al. 2012; Stumpe et al. 2012). The *TESS* data were sampled at 2-min cadence and, after removing cadences flagged as potentially affected by anomalous events, the PDCSAP flux extracted from the FITS files produced by the SPOC pipeline (grey-dotted light curves

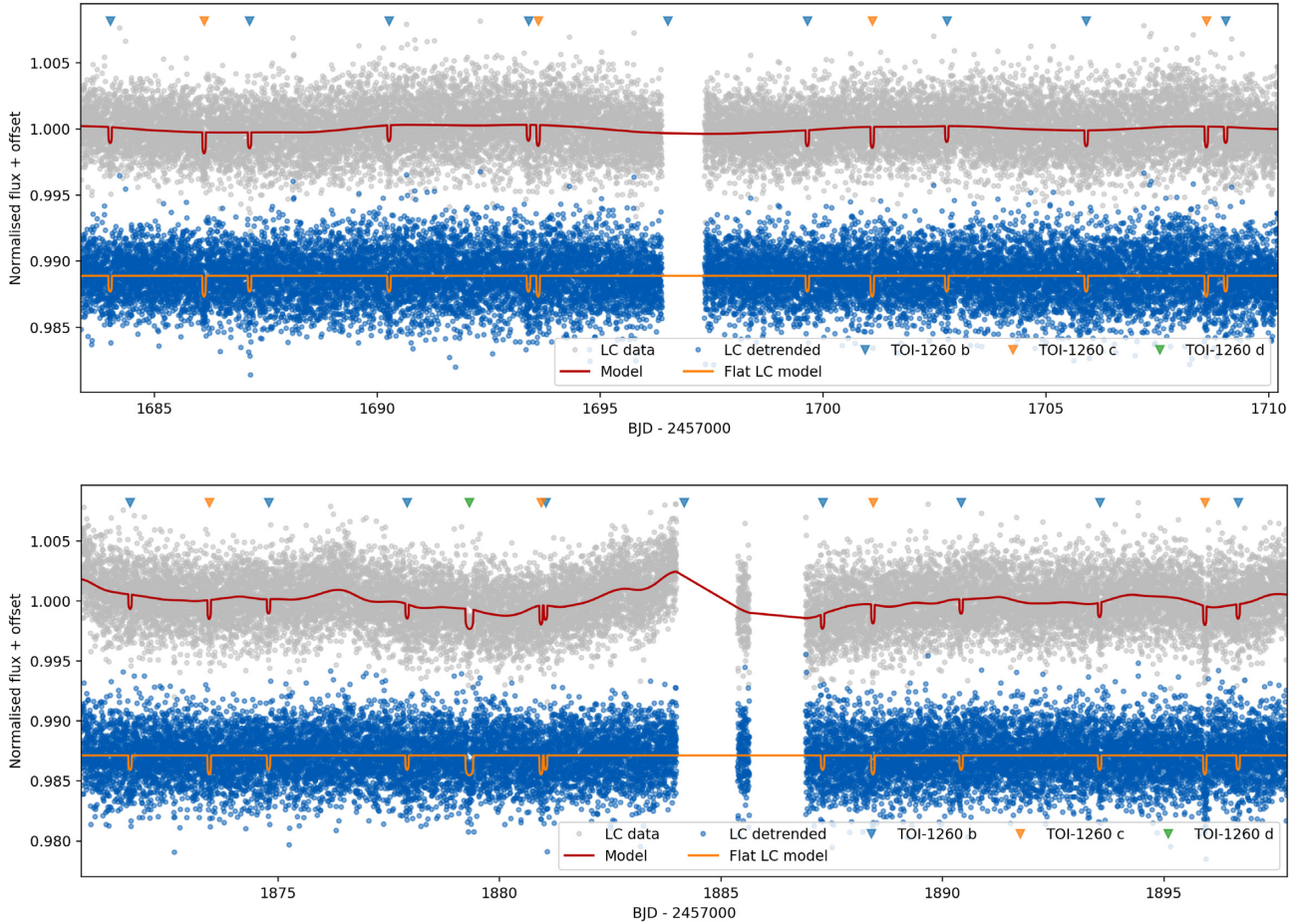


Figure 2. PDCSAP light curve in grey with GP model and transits overplotted in red, and resulting detrended light curve in blue for Sector 14 (top panel) and Sector 21 (bottom panel). The single transit event is visible in the bottom panel at 1879.3 d here plotted with a duration consistent with an arbitrary period of 40 d for visualization. Individual transits are marked with triangles.

in both panels of Fig. 2) was used for both data sets to conduct the transit search.

Our transit search was realized via the MATLAB-based package EXOTRANS (Grziwa, Pätzold & Carone 2012). EXOTRANS utilizes filtering routines based on the Stationary Wavelet Transform to remove intrinsic stellar variability as well as signals at known frequencies to allow searching for additional transits. The search itself is performed using an optimized version of the traditional well-established BLS algorithm (Kovács, Zucker & Mazeh 2002), as described in Ofir (2014). TOIs 1260.01 and 1260.02 were first discovered in the SPOC transit search (Jenkins 2002; Jenkins et al. 2010, 2017) with periods of 3.13 and 7.49 d, respectively, and announced in the *TESS* SPOC data validation reports (DVR; Twicken et al. 2018) and the TOI release portal.¹ We note that 1260.02 is missing from the DVR for Sector 21. Instead, in addition to 1260.01, a signal at 16.613 d was reported but was not given TOI status, likely due to the significant difference in depth between its two apparent transits, the second of which coincides with a transit of 1260.02. This is further discussed in Section 4.1.

EXOTRANS detected the two candidates with depths of 1222 and 1685 ppm in both *TESS* sectors, and periods in agreement with the publicly announced 1260.01 and 1260.02, respectively.

As an additional check, we further analysed the light curve data using the `lightcurve` package (Lightcurve Collaboration 2018). We discovered no significant odd/even difference or a sign of a secondary eclipse. This concurs with the results in the DVRs, where the odd/even depth test and difference image centroid test also found no evidence for either signal being due to an eclipsing binary or background eclipsing binary. Encouraged by the agreement between the different pipelines, we prioritized TOI-1260 and qualified it as a promising target for follow-up observations.

Due to the complex variability TOI-1260 exhibits, we chose to remove the low-frequency signals in the light curves using a Gaussian process (GP). We use the PYTHON package `citlalicue`,² which is a wrapper of `george` (Foreman-Mackey et al. 2014; Ambikasaran et al. 2016) and `pytransit` (Parviainen 2015). Briefly, `citlalicue` performs a GP regression (given a covariance function as provided by `george`) together with transit models (`pytransit`) to the data. The best-fitting model is computed by likelihood maximization. This generates a model that contains variability and transits. `citlalicue` then removes the light-curve variability model from the data to create a flattened normalized light curve with only transits.

¹<https://tess.mit.edu/toi-releases/>

²<https://github.com/oscaribv/citlalicue>

We ran *citlalicue* with a GP created with a Matérn 3/2 covariance function together with a model of the two transiting planet candidates and an additional single transit we identified in Sector 21 at $T_0 \sim 1879.32$. Since we are not interested in the nature of the variability signal, we chose the Matérn 3/2 kernel because of its flexibility in dealing with stochastic correlation. We performed individual runs for each sector given that light-curve variability scales may be different between the sectors.

The PDCSAP light curves of both sectors are shown in Fig. 2, along with the flattened light curves and transit models. We use these flattened light curves for our joint analysis in Section 4. The single transit is visible in the lower panel of Fig. 2 and its depth is approximately 1430 ppm. The feature is shown plotted assuming an arbitrary period of 40 d, which is within the range of possible periods for this possible outer planet (more on this in Section 4.1).

2.2 Light curve follow-up

As a further step towards confirming the planets and to try and improve the system parameters, we acquired ground-based time-series follow-up photometry of TOI-1260 as part of the *TESS* Follow-up Observing Program (TFOP).³ We used the *TESS* Transit Finder, which is a customized version of the *Tapir* software package (Jensen 2013), to schedule our transit observations. The photometric data were extracted using *AstroImageJ* (Collins et al. 2017).

2.2.1 LCOGT

We observed a full transit of 1260.01 on 2020 January 4 and parts of the 1260.02 SPOC ephemeris 3σ window on 2019 December 3 and 2020 February 1 from LCOGT 1.0-m network node at McDonald Observatory. All observations were in the Pan-STARSS z -short filter. The 4096×4096 LCOGT SINISTRO cameras have an image scale of $0''.389$ per pixel, resulting in a $26 \text{ arcsec} \times 26 \text{ arcsec}$ field of view. The 1260.01 images were defocused and have typical stellar point-spread-functions (PSFs) with full width half-maximum (FWHM) $\sim 8''.3$, and circular apertures with radius $\sim 9''.7$ were used to extract the differential photometry. Regarding both epochs of TOI 1260.02, the first observations cover a partial (half) transit, and on the second occasion the observations cover a fraction of the transit ingress. Neither data-set shows a hint of the planet signal. This can be caused by data-reduction systematics given the partial coverage of the transits and the relatively low light-curve precision. Therefore we do not use these data for further analysis. The photometry ruled out a transit on target and ruled out possible contaminating nearby eclipsing binaries (NEBs) within $2''.5$ of the target star over the observing window.

2.2.2 KeplerCam

We observed overlapping transits of TOIs 1260.01 and 1260.02 (assuming the initial SPOC Sector 14 nominal ephemerides) in Sloan i -band on 2019 November 18 from KeplerCam on the 1.2-m telescope at the Fred Lawrence Whipple Observatory. The 4096×4096 Fairchild CCD 486 detector has an image scale of $0''.336$ per pixel, resulting in a $23''.1 \times 23''.1$ field of view. The observations were focused and the resulting images have typical stellar PSFs with an FWHM of $\sim 1''.5$. Circular apertures with radius $\sim 4''.7$ were used

to extract the differential photometry. The on-target light curve was inconclusive, but possible contaminating NEBs within $2''.5$ of the target star were ruled out over the 183 min observing window.

2.3 AO with Gemini-North/NIRI

It is crucial that close visual companions are identified, since these can dilute the light curve and thus alter the planet properties, or even be the source of false positive signals, in the case that the visual companion is itself a binary (see e.g. Ciardi et al. 2015). We search for such companions using AO imaging using the NIRI instrument (Hodapp et al. 2003) at the Gemini-North telescope. We collected a total of nine images of TOI-1260 on 2019 November 25, using the narrow-band Br γ filter which falls within the K band. Each image had an exposure time of 3.9 s, and we dithered the telescope between each image. This allows for a sky background frame to be constructed from the science data itself, by median combining these dithered frames. Our data reduction process consisted of bad pixel removal, flat-correction and sky-background subtraction, and aligning the stellar position between frames so they could be coadded. We searched for companions in the final image visually, and did not identify companions anywhere in the field of view, which extends to at least 13 arcsec from the star in all directions. We used a fake star injection technique to measure the sensitivity of the data. In this process, we sequentially injected fake PSFs (constructed from the measured stellar PSF, and with peak brightness 3 times the local dispersion level) into the image, every 132 mas in the radial direction and at 8 distinct position angles for each radius. We measured the significance of each fake PSF, and linearly scale this value to the flux at which a companion would be detected with 5σ significance. The quoted sensitivity at each radius is the median sensitivity across the 8 position angles. We are sensitive to companions 5 mag fainter than the star at separations beyond 270 mas, and reach a contrast limit of $\Delta K = 7.3$ mag in the wide field. The upper panel in Fig. 3 shows the sensitivity of our survey, and the inset shows an image of the target itself.

We note that the above-described procedure has been used in a wide range of papers (see e.g. Günther et al. 2019; Kostov et al. 2019; Rodriguez et al. 2019)

2.4 Gemini-North/Alopeke speckle imaging

While AO imaging is sensitive in the infrared and at wider separations from the target, speckle imaging explores the closer vicinity of the target at optical wavelengths.

TOI-1260 was observed on 2020 February 16 using the ‘Alopeke speckle instrument on Gemini-North.⁴ ‘Alopeke provides simultaneously speckle imaging in two bands, 562 and 832 nm, with output data products including a reconstructed image, and robust limits on companion detections (Howell et al. 2011). Fig. 3 (lower panel) shows our resulting contrast curves and the reconstructed 832 nm speckle image. We find that TOI-1260 is a single star with no companion brighter than about 5–7 mag detected within $1''.2$. ‘Alopeke observations provide resulting spatial resolutions of 0.017 mas in the blue, and 0.026 mas in the red, yielding an inner working angle of 1.18 and 1.84 au at the distance to TOI-1260, respectively.

³<https://tess.mit.edu/followup>

⁴<https://www.gemini.edu/sciops/instruments/alopeke-zorro/>

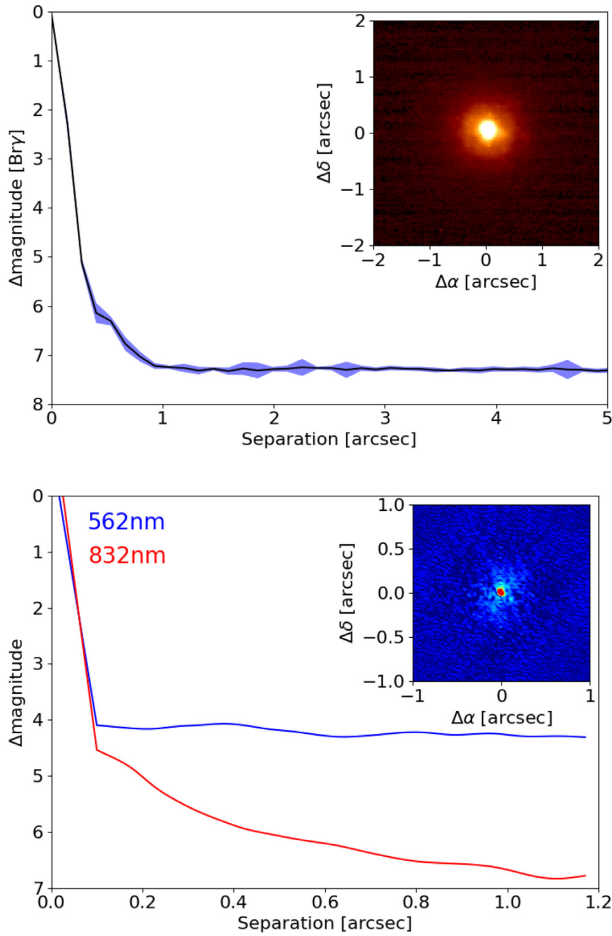


Figure 3. Upper panel: sensitivity to faint visual companions of our Gemini/NIRI observations of TOI-1260. Companions 5 mag fainter than the host star can be detected beyond 270 mas and no companions are seen anywhere in the field of view, which extends at least 13 arcsec from the target in all directions. The inset shows the central portion of the image, centred on the star, and the star appears single to the limit of our resolution. Lower panel: 5σ sensitivity curve of speckle imaging by Gemini North/Alopeke showing a reconstructed image of the field. No bright companions are detected within 1.2 arcsec.

2.5 High-dispersion spectroscopy with TNG/HARPS-N

Currently, RV measurements are invaluable for the purpose of planetary mass determination. Such observations, however, also allow for co-added stellar spectra to be obtained, which are used to model the star and thus obtain more accurate stellar parameters.

Between 2020 January 14 and 2020 June 13 we collected 33 spectra with the HARPS-N spectrograph ($R \approx 115\,000$; Cosentino et al. 2012) mounted at the 3.58-m Telescopio Nazionale Galileo (TNG) of Roque de los Muchachos Observatory in La Palma, Spain, under the observing programmes CAT19A_162, ITP19_1, and A40TAC_22.⁵ The exposure time was set to 1350–3600 s, based on weather conditions and scheduling constraints, leading to an SNR per pixel of 21–74 at 5500 Å. The spectra were extracted using the off-line version of the HARPS-N Data Reduction Software

⁵20 spectra were obtained from the Spanish CAT19A_162 programme (PI: Nowak), 12 spectra from ITP19_1 programme (PI: Pallé) and one spectrum from A40TAC_22 programme (PI: Gandolfi).

(DRS) pipeline (Cosentino et al. 2014), version 3.7. Absolute RVs and spectral activity indicators – bisector inverse slope (BIS), full-width at half maximum (CCF_FWHM), contrast (CCF_CTR) of the cross-correlation function (CCF) and Mount-Wilson S-index – were measured using an online version of the DRS, the YABI tool, by cross-correlating the extracted spectra with a K5 mask (Baranne et al. 1996). We also used *serval* (Zechmeister et al. 2018) code to measure relative RVs by the template-matching, chromatic index (CRX), differential line width (dLW), and $H\alpha$ index. The uncertainties of the RVs measured with *serval* are in the range 0.9–3.1 m s^{-1} , with a mean value of 1.6 m s^{-1} . Table A1 gives the time stamps of the spectra in BJD_{TDB}, *serval* relative RVs along with their 1σ error bars, and spectral activity indicators measured with YABI and *serval*. In the joint RV and transit analysis presented in Section 5, we used relative RVs measured from HARPS-N spectra with *serval* by the template-matching technique.

2.5.1 Frequency analysis of TNG/HARPS-N data

In order to search for the Doppler reflex motion induced by the transiting planetary candidates and unveil the presence of possible additional signals we performed a frequency analysis of the RVs and spectral activity indicators measured from TNG/HARPS-N spectra. We calculated the generalized Lomb–Scargle (GLS) periodograms (Zechmeister & Kürster 2009) of the available time series and computed the theoretical 10, 1, and 0.1 per cent false alarm probability (FAP) levels (Fig. 4). The 151.8 d time baseline of the measurements translate into a frequency resolution of 0.006586 d^{-1} .

The strongest peak in the GLS periodogram of RVs (FAP < 0.1 per cent) has a frequency of ~ 0.031 , i.e. a period of $\sim 32.5 \text{ d}$ (panel a of Fig. 4). Peaks at this frequency are also the strongest ones in the GLS periodograms of spectral activity indicators measured with the DRS pipeline, especially in the periodogram of CCF-FWHM (panel e of Fig. 4) and in the periodogram of dLW measured with *serval* (panel h of Fig. 4). The GLS periodogram of residuals after fitting two sinusoids with periods and phases corresponding to 1260.01 ($f_b = 0.320 \pm 0.002 \text{ d}^{-1}$, $P_b = 3.13 \pm 0.02 \text{ d}$) and 1260.02 ($f_c = 0.133 \pm 0.002 \text{ d}^{-1}$, $P_c = 7.49 \pm 0.11 \text{ d}$) shows two highly significant peaks (FAP < 0.1 per cent) at the frequency of $0.031^{+0.002}_{-0.003} \text{ d}^{-1}$ and its first harmonic. This clearly shows that the strongest signal in the radial velocities has its origin in stellar activity. The RV residuals after a joint model presented in Section 4 (panel c of Fig. 4) show no further significant peaks. In the GLS periodograms of the activity indicators there are no peaks at the frequencies of the candidates.

The above results show that due to the suboptimal quantity and sampling of the data, a simple periodogram inspection is not suitable for such subtle and sophisticated analysis as required by this system. For the global model, we thus implement a more advanced technique as demonstrated in Section 4.

3 STELLAR MODELLING

3.1 Spectral analysis

We modelled the co-added high resolution ($R = 115\,000$) HARPS-N spectra with a signal to noise of 125 at 5800 Å with the spectral analysis package SME (Spectroscopy Made Easy; Valenti & Piskunov 1996; Piskunov & Valenti 2017) version 5.22. This software package matches observations to synthetic stellar spectra calculated from grids of atmosphere models using a χ^2 -minimizing procedure. We

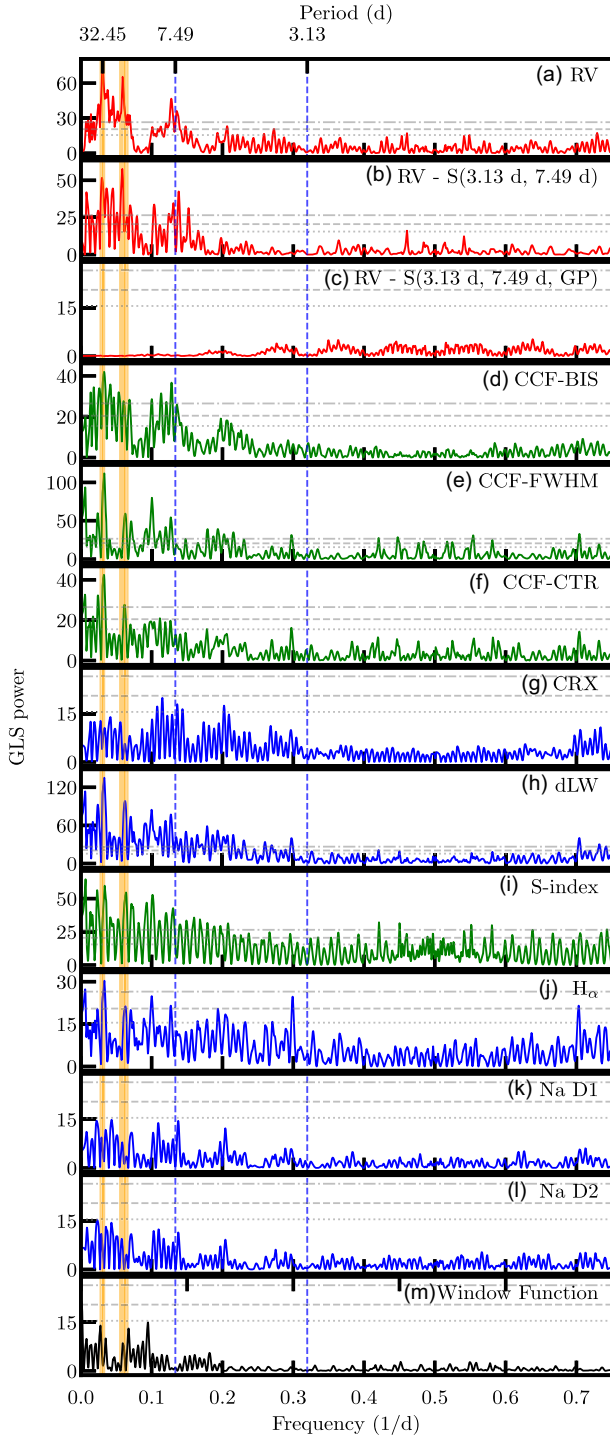


Figure 4. Generalized Lomb-Scargle periodograms of RVs of TOI-1260 (a), their residuals (b) after fitting two sinusoids with periods and phases corresponding to 1260.01 ($f_b = 0.320 \pm 0.002 \text{ d}^{-1}$, $P_b = 3.13 \pm 0.02 \text{ d}$) and 1260.02 ($f_c = 0.133 \pm 0.002 \text{ d}^{-1}$, $P_c = 7.49 \pm 0.11 \text{ d}$), marked as vertical blue dashed lines, and their residuals (c) after fitting final joint model presented in Section 4. Vertical orange areas present frequency of the GP signal ($f_{GP} = 0.031^{+0.002}_{-0.003} \text{ d}^{-1}$, $P_{GP} = 32.45^{+3.70}_{-2.14} \text{ d}$) and its first harmonic. Panels plotted in green show periodograms of spectral activity indicators measured with DRS pipeline and panels plotted in blue activity indicators measured with *servail*. Last panel (m) presents the window function of the data. Horizontal grey lines show the theoretical FAP levels of 10 (dotted line), 1 (dashed line), and 0.1 per cent (dash-dotted line) for each panel.

Table 2. Spectroscopic parameters derived with SME and SpecMatch-Emp compared to the stellar effective temperature from *Gaia*.

Method	T_{eff} (K)	[Fe/H]	$\log g$ (cgs)	$V \sin i_*$ (km s^{-1})
SME ^a	4227 ± 85	-0.10 ± 0.07	4.57 ± 0.05	1.5 ± 0.7
SpecMatch-Emp	4207 ± 70	-0.06 ± 0.12
Gaia	4351^{+204}_{-110}

^a Adopted stellar parameters.

used the MARCS 2012 (Gustafsson et al. 2008) grid and also checked the final models with the ATLAS12 model spectra (Kurucz 2013). The line data were taken from VALD (Ryabchikova et al. 2015). We derived the effective temperature (T_{eff}), the stellar surface gravity ($\log g$), abundances, the projected stellar rotational velocity ($V \sin i_*$), and the macroturbulent velocity (V_{mac}), following the procedures described in Persson et al. (2018) and Fridlund et al. (2017). In summary, we used the line wings of $H\alpha$ to derive T_{eff} , and $\log g$ was modelled with the line wings of the $\text{Ca I} \lambda\lambda 6102, 6122, \text{ and } 6162$ triplet, and the $\lambda 6439$ line. Due to the low T_{eff} , and hence the weak line wings of $H\alpha$ and the large number of metal lines contaminating the diagnostic line wings, we also used the Na doublet $\lambda\lambda 5889$ and 5896 sensitive to both T_{eff} and $\log g$ to check our model. $V \sin i_*$, V_{mac} , and the iron and calcium abundances, [Fe/H] and [Ca/H], were modelled with narrow and unblended lines between $\lambda 5600$ and $\lambda 6500$, and the [Na/H] abundance with lines between $\lambda 5600$ and $\lambda 6200$. The abundances of Ca and Na were similar to Fe. The macroturbulent and radial velocities were found to be 1.5 and -16.6 km s^{-1} , respectively, while the microturbulent velocity, V_{mic} , was fixed to 1 km s^{-1} .

To check the SME results we also used the empirical SpecMatch-Emp (Yee, Petigura & von Braun 2017) code characterizing stars based on their optical spectra. The software compares the observed spectrum to a spectral library of more than 400 well-characterized stars with spectral classes M5 to F1 observed by Keck/HIRES. Since the library stars often have their radii calibrated using interferometry, the direct output is T_{eff} , R_* , and [Fe/H]. Before running the code, we transformed our co-added HARPS-N spectra into the format of Keck/HIRES spectra used by SpecMatch-Emp as outlined in Hirano et al. (2018).

The models are in excellent agreement and we list the results in Table 2 along with the effective temperature from *Gaia* as a comparison. We adopt the SME results for the modelling of the stellar mass and radius in the following section.

3.2 Stellar mass and radius

We started with an independent determination of the stellar radius, and performed an analysis of the broad-band spectral energy distribution (SED) of the star together with the *Gaia* DR3 parallaxes adjusted by $+0.08 \text{ mas}$ to account for the systematic offset reported by Stassun & Torres (2018). We followed the procedures described in Stassun & Torres (2016) and Stassun, Collins & Gaudi (2017), Stassun et al. (2018a) and pulled the JHK_s magnitudes from the 2MASS catalogue, the W1–W4 magnitudes from the WISE catalogue, and the $GG_{BP}G_{RP}$ magnitudes from the *Gaia* database. Together, the available photometry spans the stellar SED over the wavelength range $0.4\text{--}22 \text{ } \mu\text{m}$. We performed a fit using NextGen stellar atmosphere models, with T_{eff} , [Fe/H], and $\log g$ adopted from the spectroscopic analysis with SME as priors. The only additional free parameter is the extinction (A_V), which we restricted to the maximum line-of-sight value from the dust maps of Schlegel, Finkbeiner & Davis

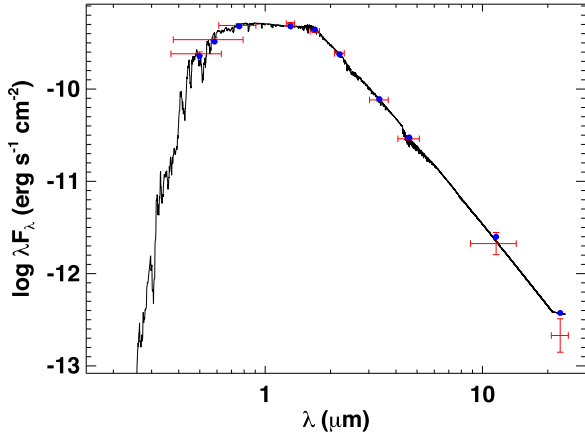


Figure 5. Spectral energy distribution of TOI-1260. Red symbols represent the observed photometric measurements, where the horizontal bars represent the effective width of the passband. Blue symbols are the model fluxes from the best-fitting NextGen atmosphere model (black).

(1998). The resulting fit, shown in Fig. 5, is very good with a reduced χ^2 of 1.1 and best fit $A_V = 0.02 \pm 0.02$. Integrating the (unreddened) SED model gives the bolometric flux at Earth, $F_{\text{bol}} = 7.63 \pm 0.18 \times 10^{-10} \text{ erg s}^{-1} \text{ cm}^{-2}$. Taking the F_{bol} and T_{eff} together with the *Gaia* DR3 parallax, gives the stellar radius. Using this radius together with the spectroscopic $\log g$, we obtain an empirical mass estimate.

In order to obtain a uniform set of stellar parameters we used the PYTHON code *isochrones* (Morton 2015), an MCMC fitting tool of stellar properties based on an interface interacting with the MIST (Choi et al. 2016) stellar evolution tracks. We fitted the *Gaia* DR3 parallax and the 2MASS *JHK* photometry, the four *WISE* magnitudes and the *B* and *V* bands from APASS, with priors on T_{eff} , $\log g$, and $[\text{Fe}/\text{H}]$ from SME using MultiNest (Buchner et al. 2014) to sample the joint posteriors. We find a bolometric luminosity of $0.139 \pm 0.005 L_{\odot}$.

The above results were checked with the Bayesian Param1.5 (da Silva et al. 2006) online code using the PARSEC isochrones (Bressan et al. 2012) and the same input as for *isochrones*.

We also computed mass and radius from the empirical calibration equations by Torres (2010) from T_{eff} , $\log g$, and $[\text{Fe}/\text{H}]$. Finally, we used the stellar mass–radius relations for low-mass stars from Boyajian et al. (2012) to compute the stellar mass from the radius obtained from *isochrones*.

The stellar parameters found above indicate that this star is a K6 V star supported by the empirical relations of Stassun et al. (2012) suggesting that the activity-driven radius inflation is at most ~ 2 percent, indicating a star on the main sequence. This is also consistent with the age estimates with Param1.5 of $8.4^{+4.7}_{-3.7}$ Gyr.

All results of the stellar mass and radius are in very good agreement and are listed in Table 3 along with a typical mass and radius for an K6 V star for comparison. We adopt the stellar mass and radius from *isochrones* in our joint modelling of the system in Section 4 and list our adopted parameters for the modelling in Table 4.

3.3 Stellar activity and rotation period

We note that both Ca II H & K lines are seen in emission in the HARPS-N spectra which indicates that the star is moderately active. The activity offers a way to estimate the rotation period. We first computed the average S-index from the time series to be 1.13 ± 0.08

Table 3. Stellar mass and radius and the corresponding stellar densities derived with different methods and typical mass and radius for an K6 V star.

Method	M_{\star} (M_{\odot})	R_{\star} (R_{\odot})	ρ_{\star} (g cm^{-3})
<i>isochrones</i> ^{a, b}	0.66 ± 0.01	0.65 ± 0.01	3.43 ± 0.08
Param1.5 ^b	0.63 ± 0.02	0.63 ± 0.02	3.53 ± 0.32
SED fitting ^b	0.61 ± 0.08^c	0.67 ± 0.03	...
SpecMatch-Emp	...	0.67 ± 0.07	...
Torres ^{b, d}	0.61 ± 0.04	0.65 ± 0.05	3.07 ± 0.68
Boyajian ^e	0.65 ± 0.04
Light curve model ^f	$3.46^{+0.62}_{-0.93}$
Spectral type K6 V ^g	0.66	0.65	3.39

^aAdopted stellar mass and radius in the modelling in Section 4.

^bUsing T_{eff} , $\log g$, and $[\text{Fe}/\text{H}]$ from SME.

^cCombining the SED radius with $\log g$.

^dTorres (2010) calibration equations.

^eBoyajian et al. (2012) calibration equation from eclipsing binaries using R_{\star} from *isochrones*.

^fStellar density obtained from the light curve model (Section 4).

^gTypical mass and radius for a K6 V star.

which was converted to $\log(R'_{HK}) = -4.86 \pm 0.03$ (Suárez Mascareño et al. 2015). This was used together with the empirical relation for late-type stars from Suárez Mascareño et al. (2015, 2016) and the star’s colour to predict a rotation period of 34 ± 2 d. This is within 1σ of the 22 ± 10 d estimate obtained from R_{\star} together with the spectroscopically determined $V \sin i_{\star}$, assuming that the star is equator-on oriented.

The activity predicts an age of 4.1 ± 0.2 Gyr, from the empirical relations of Mamajek & Hillenbrand (2008) which is considerably lower than derived above although still within the large uncertainties. The estimate from gyrochronology has, however, the following two caveats: this star is somewhat cooler than the nominal range of applicability of the relations, and secondly, recent work have suggested that K-dwarfs experience a stall in their spin-down (Curtis et al. 2020), so that such stars can be considerably older than their observed rotation or activity may otherwise suggest.

3.4 Population membership

The kinematics of this high proper motion star can be used to compute probabilities of membership in different populations in the Galaxy. Using the data in Table 1 and the methodology of Reddy, Lambert & Allende Prieto (2006), we find galactic velocity components of $U = -43.42$, $V = -45.96$, $W = -30.95 \text{ km s}^{-1}$. We converted these velocities to the local standard of rest of the Sun to $U_{\text{lsr}} = -33.42 \pm 0.16$, $V_{\text{lsr}} = -40.66 \pm 0.12$, and $W_{\text{lsr}} = -23.75 \pm 0.15 \text{ km s}^{-1}$. This results in a probability of the star belonging to the thin disc population of $P(\text{thin}) = 0.95 \pm 0.02$, and to the thick disc $P(\text{thick}) = 0.0516 \pm 0.0002$, and a vanishingly low probability of the star being old enough to belong to the halo population. The thin disc of the Galaxy is expected to have formed 8.8 ± 1.7 Gyr ago (del Peloso et al. 2005) which is consistent with the derived ages.

4 JOINT RV AND TRANSIT ANALYSIS

We use the open source software *pyaneti* (Barragán, Gandolfi & Antoniciello 2019a), which uses a Bayesian approach with MCMC sampling for planetary systems parameter estimation, to perform our joint transit and RV analysis, as well as the monotransit and multiband fits.

Table 4. Summary of the system parameters from the stellar modelling in Section 3 and the joint RV and transit modelling with `pyaneti` in Section 4.

Parameter	Prior ^a	Value ^b
Model Parameters for TOI-1260		
<i>TOI-1260 b</i>		
Orbital period P_{orb} (d)	$\mathcal{U}[3.1270, 3.1280]$	$3.12748^{+0.000047}_{-0.000038}$
Transit epoch T_0 (BJD – 2,450,000)	$\mathcal{U}[8684.0050, 8684.0250]$	$8684.0128^{+0.0016}_{-0.0024}$
e	$\mathcal{F}[0]$	0
ω_*	$\mathcal{F}[\pi/2]$	$\pi/2$
Scaled planetary radius R_p/R_*	$\mathcal{U}[0.01, 0.10]$	$0.0329^{+0.0014}_{-0.0012}$
Impact parameter, b	$\mathcal{U}[0, 1]$	$0.26^{+0.25}_{-0.17}$
Radial velocity semi-amplitude variation K (m s ⁻¹)	$\mathcal{U}[0, 25]$	$4.91^{+0.77}_{-0.83}$
<i>TOI-1260 c</i>		
Orbital period P_{orb} (d)	$\mathcal{U}[7.4925, 7.4940]$	$7.49325^{+0.00015}_{-0.00013}$
Transit epoch T_0 (BJD – 2450 000)	$\mathcal{U}[8686.1050, 8686.1300]$	$8686.1179^{+0.0033}_{-0.0035}$
e	$\mathcal{F}[0]$	0
ω_*	$\mathcal{F}[\pi/2]$	$\pi/2$
Scaled planetary radius R_p/R_*	$\mathcal{U}[0.01, 0.10]$	0.0398 ± 0.0020
Impact parameter, b	$\mathcal{U}[0, 1]$	$0.714^{+0.067}_{-0.066}$
Radial velocity semi-amplitude variation K (m s ⁻¹)	$\mathcal{U}[0, 25]$	5.1 ± 1.4
GP Period P_{GP} (d)	$\mathcal{U}[22, 43]$	$32.5^{+3.7}_{-2.2}$
λ_p	$\mathcal{U}[0.1, 5]$	$1.4^{+1.0}_{-0.5}$
λ_e (d)	$\mathcal{U}[1, 200]$	45^{+17}_{-16}
V_c (km s ⁻¹)	$\mathcal{U}[0, 0.1]$	$0.005^{+0.012}_{-0.004}$
V_r (km s ⁻¹)	$\mathcal{U}[0, 1]$	$0.22^{+0.32}_{-0.12}$
S_c	$\mathcal{U}[0, 1]$	$0.26^{+0.28}_{-0.12}$
Offset HARPS-N (km s ⁻¹)	$\mathcal{U}[-0.05, 0.05]$	$0.0046^{+0.0050}_{-0.0057}$
Offset S-index	$\mathcal{U}[0.5, 1.9]$	1.11 ± 0.17
Jitter term $\sigma_{\text{HARPS-N}}$ (m s ⁻¹)	$\mathcal{J}[10^{-3}, 10^{-1}]$	$0.88^{+0.83}_{-0.61}$
Jitter term $\sigma_{\text{S-index}}$	$\mathcal{J}[10^{-3}, 10^{-1}]$	$0.0431^{+0.0088}_{-0.0070}$
Limb darkening q_1 , <i>TESS</i>	$\mathcal{U}[0, 1]$	$0.44^{+0.33}_{-0.24}$
Limb darkening q_2 , <i>TESS</i>	$\mathcal{U}[0, 1]$	$0.36^{+0.31}_{-0.24}$
Limb darkening q_1 , LCO	$\mathcal{U}[0, 1]$	$0.35^{+0.39}_{-0.24}$
Limb darkening q_2 , LCO	$\mathcal{U}[0, 1]$	$0.42^{+0.32}_{-0.28}$
Jitter term σ_{TESS} ($\times 10^{-6}$)	$\mathcal{U}[0, 1 \times 10^3]$	752 ± 27
Jitter term σ_{LCO} ($\times 10^{-6}$)	$\mathcal{U}[0, 1 \times 10^3]$	141^{+15}_{-99}
Stellar density ρ_* (g cm ⁻³)	$\mathcal{U}[0.1, 10]$	$3.47^{+0.89}_{-1.22}$
Derived parameters		
TOI-1260 b		
Planet mass (M_{\oplus})	$8.6^{+1.4}_{-1.5}$	$11.8^{+3.4}_{-3.2}$
Planet radius (R_{\oplus})	$2.34^{+0.11}_{-0.09}$	2.82 ± 0.15
Planet density (g cm ⁻³)	$3.69^{+0.81}_{-0.76}$	$2.87^{+0.98}_{-0.86}$
Scaled semimajor axis a/R_*	$12.14^{+0.7}_{-1.2}$	$21.7^{+1.2}_{-2.2}$
Semimajor axis a (au)	$0.0366^{+0.0022}_{-0.0036}$	$0.0656^{+0.0039}_{-0.0065}$
Orbital inclination i (deg)	$88.8^{+0.8}_{-1.4}$	$88.12^{+0.24}_{-0.39}$
Transit duration t_{tot} (h)	$1.963^{+0.066}_{-0.091}$	$1.96^{+0.12}_{-0.10}$
Equilibrium temperature $^c T_{\text{eq}}$ (K)	860^{+47}_{-31}	643^{+35}_{-23}
Insolation F_p (F_{\oplus})	91^{+22}_{-12}	$28.4^{+6.8}_{-3.9}$
Planet surface gravity ^d (cm s ⁻²)	1520^{+370}_{-420}	1410^{+550}_{-500}
Planet surface gravity (cm s ⁻²)	1540 ± 290	1450^{+450}_{-410}
Adopted stellar parameters		
Stellar mass (M_{\odot})	...	0.66 ± 0.01
Stellar radius (R_{\odot})	...	0.65 ± 0.01
Stellar density (g cm ⁻³)	...	3.43 ± 0.08

Table 4 – *continued*

Parameter	Prior ^a	Value ^b
Effective temperature (K)	...	4227 ± 85
Bolometric luminosity (L_{\odot})	...	0.139 ± 0.005

^a $\mathcal{U}[a, b]$ refers to uniform priors between a and b , $\mathcal{J}[a, b]$ to modified Jeffrey’s priors calculated using equation (16) in Gregory (2005), and $\mathcal{F}[a]$ to a fixed value a .

^b Inferred parameters and errors are defined as the median and 68.3% credible interval of the posterior distribution.

^c Assuming an albedo of 0.

Adopting the flattened *TESS* light curves derived from `cit-lalique` (Section 2.1), together with the LCO single transit data available for 1260.01 (Section 2.1), we model the transits using the Mandel & Agol (2002) approach as implemented in `pyaneti`. We sample for the limb-darkening parameters utilizing the parametrization q_1 and q_2 described by Kipping (2013). Instead of sampling for the scaled semimajor axis, a/R_* , for each candidate, we sampled for the stellar density ρ_* , as parametrized in `pyaneti`.

Section 3.3 describes that our RV measurements contain stellar-induced RV variations. For this reason we use the multidimensional Gaussian-process approach described in Rajpaul et al. (2015) to model our RVs. This approach has been used successfully to separate planet signals from stellar activity by e.g. Barragán et al. (2019b) and Mayo et al. (2019). Briefly, it models RVs together with the activity indicators assuming the same underlying GP, $G(t)$, can describe them. This approach constrains the GP flexibility that could remove planet-induced signals. $G(t)$ can be interpreted as representing the fraction of the visible stellar disc that is covered by active regions at a given time.

For our final GP analysis, we model our RVs alongside the S-index as

$$\begin{aligned}\Delta RV &= V_c G(t) + V_r \dot{G}(t), \\ \Delta S_{\text{HK}} &= S_c G(t),\end{aligned}\quad (1)$$

respectively. The variables V_c , V_r , and S_c , are free parameters which relate the individual time series to the Gaussian Process $G(t)$. The RVs depend on the fraction of the stellar disc covered by active regions as well as how these regions move on the surface. For this reason RVs are modelled as a function of $G(t)$ and its time derivative. We use the S-index given that it is an activity indicator that depends on the fraction of the stellar disc covered by active regions, i.e. it can be described by $G(t)$ only. We use the quasi-periodic covariance function

$$\gamma(t_i, t_j) = \exp \left[-\frac{\sin^2[\pi(t_i - t_j)/P_{\text{GP}}]}{2\lambda_p^2} - \frac{(t_i - t_j)^2}{2\lambda_e^2} \right], \quad (2)$$

where P_{GP} is the period of the activity signal, λ_p the inverse of the harmonic complexity, and λ_e is the long-term evolution time-scale.

Before committing to a final model setup, we tested different orbital scenarios including two circular orbits, two eccentric orbits, as well as a combination of the two – inner body with eccentric, outer body with circular orbit, and vice versa. We found that all fits including eccentric orbits provide a solution for the eccentricities consistent with zero. We also calculated the commonly used Bayesian Information Criterion (BIC) and found that the case of two circular orbits is strongly favoured with a $\Delta\text{BIC} = 15$ better than the second best model. This is also consistent with short circularization time-scales for short-period planets as well as the Van Eylen et al. (2019) finding that multiplanet systems tend to feature low eccentricities. Since both candidates are in close-in orbits, the circular case for both yields a value for the stellar density most consistent with the

spectroscopically derived one, and given that the current data do not favour the solution with eccentric orbits, we use the circular orbits case scenario as our final model.

Using the above setup and the RVs from `serval`, we ran our final model with 500 chains to sample the parameter space. For the burn-in phase we used the last 5000 of the converged chains with a thin factor of 10, leading to a final number of 250 000 independent points for each sampled parameter.

As an additional test, we ran a joint model without accounting for the stellar signal in any way. We find that the two planets are still detected, but the HARPS-N jitter is significantly higher (8.8 m s^{-1}) than the nominal night-to-night variation ($\approx 0.8 \text{ m s}^{-1}$). This points to the presence of additional signals not accounted for by this model. Nevertheless, the results of this test agree within 1σ , thus lending confidence in our choice of final model.

To ensure that our detection is not due to an artefact of the RV data reduction, as an extra check we performed our final model setup using the DRS-derived RVs. The results once again agree to within 1σ of our adopted parameters.

Lastly, to check that our results do not depend on the sampling algorithm, we used the code `juliet` (Espinoza, Kossakowski & Brahm 2019) to model jointly the photometric and Doppler data. The algorithm is built on many publicly available tools for the modeling of transits (`batman`, Kreidberg 2015), RVs (`radvel`, Fulton et al. 2018), and GP (`george`, Ambikasaran et al. 2016; `celerite`, Foreman-Mackey et al. 2017), and computes efficiently the Bayesian log-evidence using the importance nested sampling included in the `dynesty` package (Speagle 2020). We use the same set of priors presented in Table 4, but for the GP we use an exponential-sine-squared kernel of the form $k_{i,j} = \sigma_{\text{GP,RV}}^2 \exp \left(-\alpha_{\text{GP,RV}}(t_i - t_j)^2 - \Gamma_{\text{GP,RV}} \sin^2 \left[\frac{\pi|t_i - t_j|}{P_{\text{rot;GP,RV}}} \right] \right)$ with a uniform prior in $P_{\text{rot;GP,RV}}$ ranging from 22 to 43 d. The `juliet` package does not have the possibility to perform fits with multi-dimensional GP so in this case we apply it only on the RV data. Nevertheless, the fitted parameters from the joint fit with `juliet` are in perfect agreement with the results from `pyaneti`, confirming the robustness of the different analyses and the derived orbital parameters.

A summary of our results, including the fitted parameters and priors are presented in Table 4. Fig. 6 shows the RV and S-index timeseries together with the inferred models. It should be noted that in Fig. 6 the uncertainties of the inferred models (shadow regions) are relatively large, which is caused by the sub-optimal sampling of the data and the flexibility of the GP model. This figure illustrates the usefulness of the multidimensional GP used in this work as it is clear how the RV GP model is constrained by the changes in the S-index (similar to fig. 2 of Barragán et al. 2019b).

Fig. 6 also shows phase-folded RV data of planets b (1260.01) and c (1260.02) together with the corresponding inferred RV model, while Fig. 7 shows the single transit event of planet b detected by LCO as well as the phasefolded transits of both planets as obtained from *TESS* photometry.

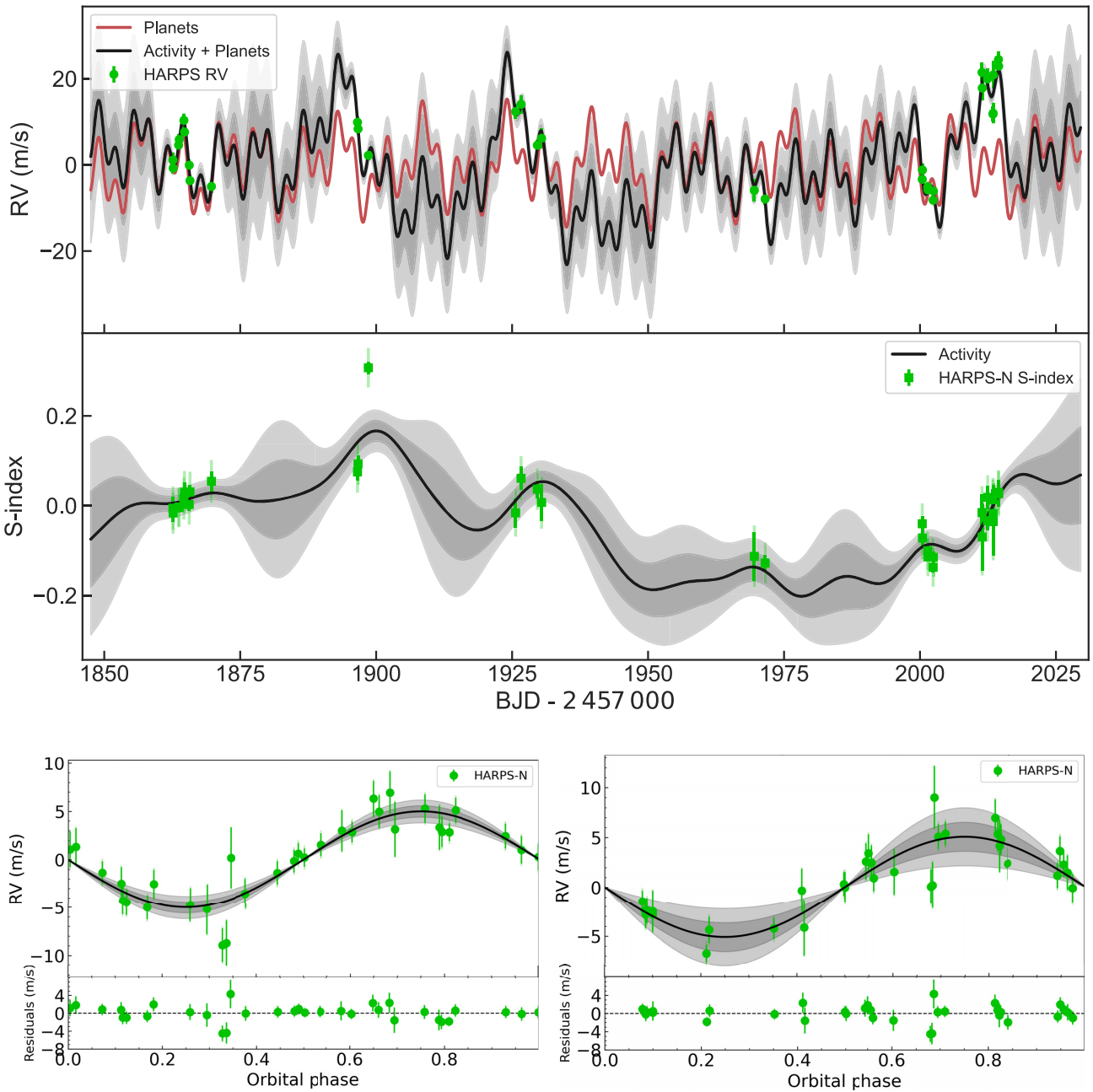


Figure 6. RV (top panel) and S-index (middle panel) time-series. The green markers in each panel represent the HARPS-N RV and S-index measurements with inferred offsets extracted. The solid dark line shows the inferred Multi-GP model, with dark and light shaded areas showing the 1σ and 2σ credible intervals of the corresponding GP model. These regions represent ranges in which other GP curves could also explain the data, with different probability. For the RV panel, we also included the RV model for the two planets (solid red line). Bottom panel: HARPS-N RV data folded on the orbital period of each candidate following the subtraction of the systemic velocities, GP signal, and the other planet. The plots also show the inferred RV model for each planet (solid black line) with 1σ and 2σ credible intervals (shaded areas). In all the plots the nominal error bars are in green, and the error bars taking into account the jitter ($\sigma_{\text{HARPS-N}}$) are semitransparent green. The latter are $<1 \text{ m s}^{-1}$ for the RV data and are hardly visible.

4.1 Tentative outer planet

As discussed in Section 2.1, we report an additional transit-like event in Sector 21. A counterpart of this feature is not visible in Sector 14, although it is possible that the transit occurred during the ~ 1 -d data gap between orbits (Fig. 2). This transit-like feature does not coincide with a spacecraft momentum dump.

To model the monotransit, we again turn to `pyanet.i`. We follow a similar approach as in Osborn et al. (2016). Assuming a circular

orbit and based on the transit shape, our single-transit model (Fig. 8) gives a range of physically possible periods of $[13.4, 56.3]$, a transit depth of 1418^{+317}_{-248} ppm, which in turn yields a radius of $2.67^{+0.29}_{-0.25} R_{\oplus}$. We further narrowed down the period range based on the length of *TESS* observations and the apparent lack of occurrence of another such transit event during the observing windows. Our final possible periods are listed in Table B1. The binned and unbinned transit data and inferred model of the aforementioned monotransit visible in Sector 21 are displayed in Fig. 8.

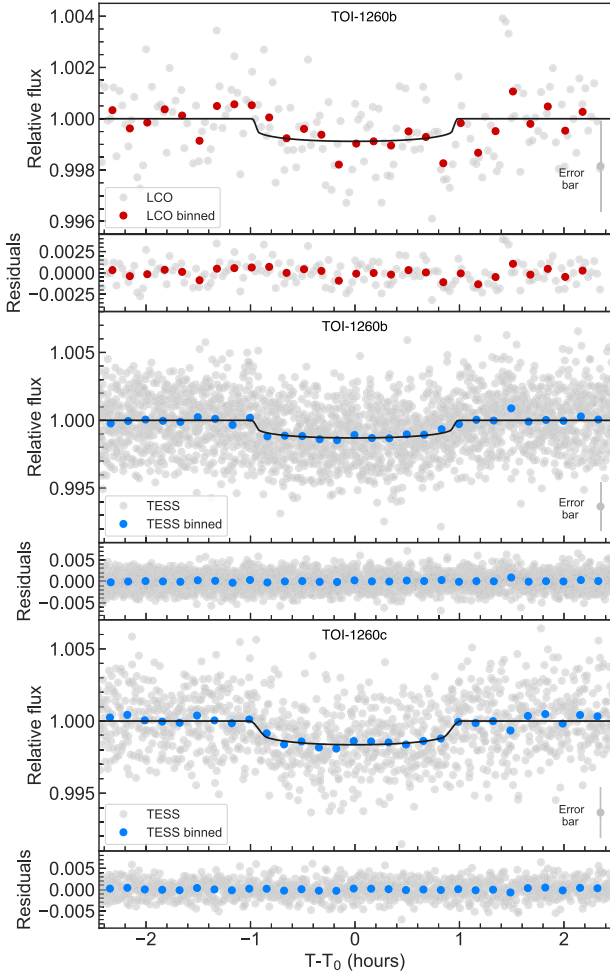


Figure 7. TOI-1260 b and TOI-1260 c transits. The panels show a flattened LCOGT and *TESS* light curves with residuals folded to the orbital periods of the planets. Black lines show the best-fitting transit models. The LCO and *TESS* radius estimates for planet b agree to nearly 1σ . Data are shown in the nominal 2-min cadence mode and binned to 10 min. Typical error bar for nominal data is shown at the bottom right for each panel.

In an attempt to try and explore further the physical properties of this tentative outer planet, we performed an MCMC analysis identical to our adopted one, but we added an extra planetary signal with ephemeris corresponding to the transit of the tentative planet d. We used a prior on T_0 of [8879.2, 8879.4], and a wide prior on the period of [20.0, 70.0] and created marginalized posterior distributions using *pyanet.i*. We were unable to further constrain the period but we found the maximum allowed semi-amplitude to be 18.4 m s^{-1} (99 per cent confidence interval).

We cannot constrain this further as there is also no sign of another planet in our RV data-set. However, with a maximum semi-amplitude of 18.4 m s^{-1} , this translates to a mass of $76.3 M_{\oplus}$. Therefore, if the signal at 1879.32 d is caused by a transiting object, this object belongs to the planetary mass domain.

We further note that the minimum period shown in Table B1 is 20.3 d. This constraint comes from the minimum period that the tentative outer planet has to have in order to not be observed transiting again in the light curve. We however, note that there is a transit of TOI-1260 c between the range 8895.80–8896.05 BJD – 2450000 that looks significantly deeper. This can be caused by some unknown systematics in the light curve or another obscuring object.

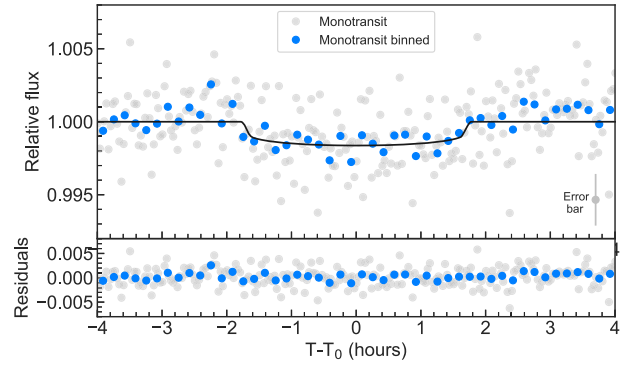


Figure 8. The single transit of the tentative outer planet d seen in Sector 21. The *pyanet.i* transit model yields a T_0 of $1879.3211^{+0.0067}_{-0.0055}$ d and a depth of 1418^{+317}_{-248} ppm, which corresponds to a radius of $2.67^{+0.29}_{-0.25} R_{\oplus}$. Data are shown in the nominal 2-min cadence mode and binned to 10 min, with typical error bar for nominal data in the bottom right.

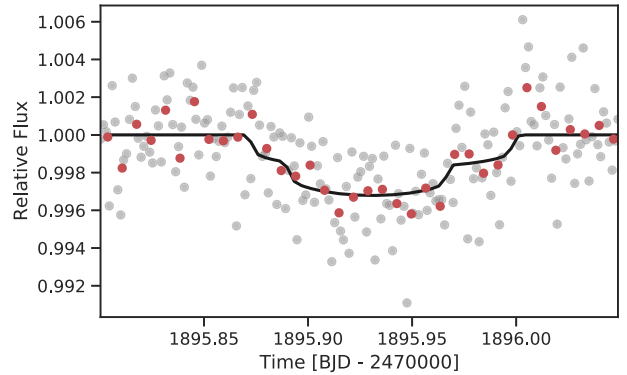


Figure 9. Two-transit model of the potentially overlapping transits of planet c and the tentative planet d, around 1895.95 BJD – 2457000. Grey circles show the flattened *TESS* data, with 10-min bins as red circles, and solid line showing the inferred transit model including both planet signals.

To investigate this, we performed a simple model adding an extra single transit to a model of planet c between the range 8895.80–8896.05 BJD – 2450000. We thus found that we obtain a better model to the data if we add a signal with a time of mid-transit of 8895.938 ± 0.005 , depth of 1705 ± 350 ppm, and transit duration of 2.9 ± 0.3 h. Fig. 9 shows a plot with the two-transit model. These tentative transit parameters are consistent within 2σ with our single transit event at 8879.3210683 BJD – 2450000. If this detected signal is real and it corresponds to a second transit of the tentative planet d, then its period would be ~ 16.61 d (see Section 2.1). Unfortunately, with this period, the only other visible transit in the available *TESS* light curves would have fallen in the data gap of Sector 14.

We then repeat a similar approach as the one described in Section 4, with an extra Keplerian signal with a tight prior on the ephemeris of the tentative 16.61-d planet but we have no clear detection of a RV signal at that period. If this planet is real, based on this three-planet model, its period, radius and transit duration would be $16.613^{+0.008}_{-0.006}$ d and $2.75^{+0.172}_{-0.177} R_{\oplus}$ and $3.11^{+0.20}_{-0.15}$ h, respectively. The 99 per cent credible interval for the maximum semi-amplitude would be around 13 m s^{-1} , which in turn translates to a maximum mass of around $39 M_{\oplus}$. Adding this signal has an insignificant effect on the parameters of planet b, while planet c shows a slight decrease in radius to $2.68 \pm 0.14 R_{\oplus}$ and an increase in mass to $13.39^{+3.49}_{-3.26} M_{\oplus}$. Both of these agree well with our officially reported estimates in Table 4.

Based on these results, we take a conservative approach and we conclude that, based on the available information, we cannot claim a planet with a period of 16.61 d. However, if there is such a planet, it could be confirmed by photometric ground or space-based follow-up. Fortunately, *TESS* will observe TOI-1260 again in three more sectors – 41, 47, and 48. We note, however, that a RV follow-up would be more challenging because this tentative period is close to half the rotation period of the star.

5 DISCUSSION

5.1 Dynamical stability

The dynamical viability of multiplanet systems is an important component of assessing valid architectures. Testing dynamical integrity and subsequent orbital evolution has played a key role in understanding Kepler systems (Lissauer et al. 2011; Li et al. 2014; Kane 2015, 2019). To test the stability of the orbital solution for our two confirmed planets in the TOI-1260 system, we executed N -body integrations using the Mercury Integrator Package (Chambers 1999). We adopted the stellar, planetary masses, and semimajor axes from Table 4. We further assumed initial circular orbits for both of the planets. The simulation was performed for 10^7 simulation years with a time-step of 0.1 d to properly sample the relatively short orbital period of the inner planet. The results of the simulation showed no signs of instability, and the eccentricities of both planets remained below 10^{-3} for the duration of the simulation. This demonstrates that the gravitational well of the star is the overwhelmingly dominant influence on the planetary dynamics within their compact system configuration. Given the proximity of the planets to each other, we also investigated the possibility of determining upper mass limits that retain dynamical stability. We gradually increased the masses of both planets independently until the dynamical integrity of the system was compromised during a series of 10^6 -yr simulations. These simulations showed that the maximum masses for both planets are loosely constrained based on their dynamical interactions, with maximum masses approaching several Jupiter masses before significant instability occurs.

Tipped off by the suspected presence of an outer planet, we decided to check if the system exhibits Transit Timing Variations (TTVs). We performed a TTV analysis using *PyTTV* (Python Tool for Transit Variations; Korth 2020), which showed that a linear ephemeris can be fit between the sectors. The ephemerides from our modelling results (Table 4) and the lack of TTVs allows for future observations of the system using other facilities to be scheduled efficiently.

5.2 Characterization of the TOI-1260 planets

Two important factors that influence the radius distribution of planets are the semimajor axis and the mass of the host star (Fulton & Petigura 2018; Wu 2019; Cloutier & Menou 2020; Van Eylen et al. 2021). Both of these determine a planet's X-ray/UV irradiation evolution. Since the magnitude and evolution of the X-ray luminosity differs between sun-like and low-mass stars (2019a; Luque et al. 2021), we show in Fig. 10 a mass–radius diagram with planets orbiting mid-M to mid-K stars (here defined as having T_{eff} between 3000 and 4400 K) measured to a precision better than 30 per cent in mass and 10 per cent in radius. We also plot theoretical models of planet core compositions without an atmosphere (Zeng et al. 2016) and with an atmosphere (Zeng et al. 2019) at different equilibrium temperatures matching TOI-1260 b and TOI-1260 c. From Fig. 10, we see that the two mini-Neptunes in the TOI-1260 system may be

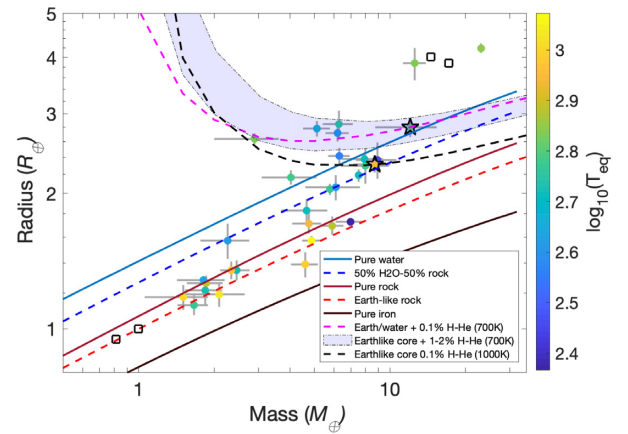


Figure 10. Mass-radius diagram of planets with measured masses better than 30 per cent and radii better than 10 per cent orbiting mid-M to mid-K dwarfs (3000–4400 K). In total there are 26 planets in 19 multiplanet systems. Models of core compositions without atmosphere (Zeng et al. 2016) and with atmosphere (Zeng et al. 2019) at different equilibrium temperatures are also plotted. TOI-1260 b and TOI-1260 c are marked with star symbols, and squares are the Solar system planets.

water worlds or rocky worlds with H–He atmospheres inflating their radii. The position of TOI-1260 b in the diagram is consistent with a planet composition of 50 per cent Earth-like rocky core (32.5 per cent Fe + 67.5 per cent MgSiO_3) and 50 per cent H_2O ice without an atmosphere, or an Earth-like rocky core with an H–He atmosphere of ~ 0.1 per cent. The position of TOI-1260 c, with $11.8^{+3.4}_{-3.2} M_{\oplus}$, $2.82 \pm 0.15 R_{\oplus}$, and a bulk density of $2.87^{+0.98}_{-0.86} \text{ g cm}^{-3}$, lies above the pure water line in the diagram. The orbital period and equilibrium temperature are 7.493 days and 643 K, respectively. We find that two models fit the position in the diagram: an Earth-like rocky core with a H–He atmosphere of ~ 2 per cent, or alternatively, a core composed of a mix of 49.95 per cent rock and 49.95 per cent ices and a H–He atmosphere of ~ 0.1 per cent.

Since the location of the photoevaporation valley is a function of stellar mass and is thus different for low-mass versus solar-type stars, we plot in Fig. 11 the same T_{eff} ranges as in Fig. 10. As evident from Fig. 11, both TOI-1260 planets lie above the photoevaporation gap (Van Eylen et al. 2018; Cloutier & Menou 2020; Van Eylen et al. 2021), or close to its edge as is the case of planet b. Depending on the photoevaporation valley fit used, however, planet b could also lie exactly in the transition zone (Wu 2019). It should be noted that the Van Eylen et al. (2018) curve is based on hotter (4700 – 6500 K) and thus higher mass stars, the Cloutier & Menou (2020) and Wu (2019) curves relate to low-mass stars (mid-K and cooler), while the Van Eylen et al. (2021) refers to M dwarfs with $T_{\text{eff}} < 4000$ K. We have colour coded the planet bulk densities in Fig. 11, and it is evident that the planets above the radius gap have lower densities than the planets below. The TOI-1260 planets are consistent with this trend as they have relatively low densities and their compositions are degenerated. They both are consistent with both (a) an Earth-like composition of iron and silicates, and (b) an Earth-like core with a substantial fraction of water ice. We delve into possible reasons for this ambiguity in the following sections.

5.2.1 Mass and radius evolution induced by photoevaporation

In order to shed light on which planet composition model TOI-1260 b and TOI-1260 c belong to, we investigate the mass and

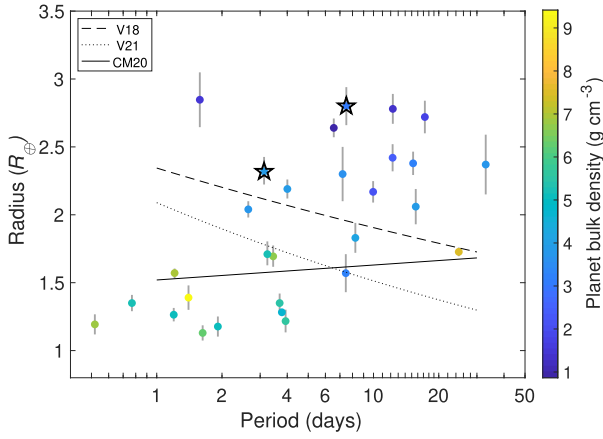


Figure 11. Radius-period diagram for the same planet population as in Fig. 10. The dashed line is the fit to the FGK radius valley from V18 (Van Eylen et al. 2018), the solid line refers to stars ≤ 4700 K as per CM20, Cloutier & Menou (2020), while the dotted line – to M dwarfs with $T_{\text{eff}} < 4000$ K (Van Eylen et al. 2021). TOI-1260 b and TOI-1260 c are again marked with star symbols. Planet c is found comfortably above all three radius valleys fits, while planet b lies on the edge of the V18 fit.

radius temporal evolution induced by atmospheric photoevaporation. To this end, we study the temporal evolution of the high-energy stellar radiation and the planetary radius. We consider a primary H–He atmosphere, a rock/iron core as per Lopez & Fortney (2014), assume circular orbits, ignore any migration effects and follow the hydrodynamic-based approximation developed by Kubyshkina et al. (2018). A major driver behind atmospheric hydrodynamic mass loss is the X-ray luminosity since X-ray heating from the star can drive a system to an intense hydrodynamic escape phase (Erkaev et al. 2007; Penz, Micela & Lammer 2008a; Locci, Cecchi-Pestellini & Micela 2019). We estimated the current X-ray luminosity using the $\log(R'_{\text{HK}})$, our SED bolometric luminosity and the relationships in Houdebine et al. (2017), obtaining $L_X = 4.51 \times 10^{27} \text{ erg s}^{-1}$. Since the evolution of extreme ultraviolet radiation follows the evolution of X-ray radiation, we accounted for the X-ray luminosity evolution by using the prescriptions given in Penz, Micela & Lammer (2008b) and the relation given in Sanz-Forcada et al. (2011). Following Poppenhaeger, Ketzner & Mallonn (2021), we account for the evolution of the planetary radius by means of the analytic fit given in Lopez & Fortney (2014). The analytic fit provides the radius envelope, R_{env} , as a function, among other parameters, of the atmospheric mass fraction, f_{atm} , and the age of the system, which in turn allows us to also account for gravitational shrinking.

Calculating the planetary mass (M_p), f_{atm} and R_{env} is an iterative process. As a first step, we look at the future evolution of the system from its present age (~ 8.4 Gyr) to 15 Gyr and assume f_{atm} values of 0.1 per cent and 2 per cent for planets b and c, respectively. These correspond to the composition scenarios of an Earth-like rocky core with an H–He envelope for both planets. We then calculate the corresponding R_{env} and estimate the core radius simply as the difference between the measured by photometry planetary radius, R_p (Table 4) and the calculated R_{env} . Next, we updated f_{atm} and M_p at each time-step according to the mass-loss and used them to calculate a new R_{env} , adding the latter to the core radius, to finally obtain the new R_p . We find that planet b loses its atmosphere in about 100 Myr, while planet c retains part of it until the end of the run.

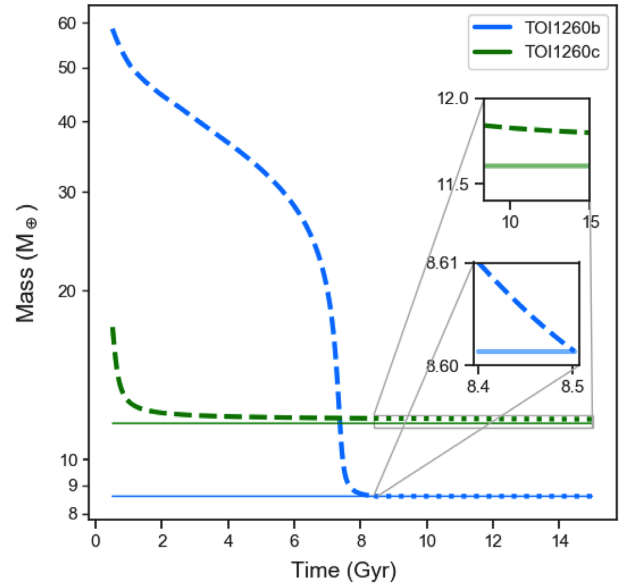


Figure 12. Mass temporal evolution of the TOI-1260 planets assuming a nominal stellar age of 8.4 Gyr, a rock/metal core and an H–He envelope of 0.1 and 2 per cent for planets b and c, respectively. Dotted lines refer to the evolution from the current age of the system until 15 Gyr. Dashed lines refer to the inferred evolution from early to current times. The insets show a zoomed-in view of the future evolution, where the semitransparent solid lines denote the core mass of each planet. It can be clearly seen that planet b would lose a 0.1 per cent H–He atmosphere in about 100 Myr, while the atmosphere of planet c is stable against photoevaporation.

5.2.2 Effect of the stellar age

To better understand the situation, we take this analysis one step further by tracing the system’s evolution back in time. Assuming the aforementioned scenarios, since the core does not change in size or mass, we create a synthetic population of planets and assign to them the current core radii and masses of our planets. This leaves f_{atm} to dictate the total mass, while the total radius is again based on the analytical fit by Lopez & Fortney (2014). We then looked at the planets that ended up with a similar current mass, radius and f_{atm} and looked at their predicted past histories.

Fig. 12 shows the result of both the future (dotted lines) and past (dashed) simulation runs. We trace the planets back to 0.5 Gyr from the assumed birth of the system and see that in the case of planet b (purple curve), we reach a mass of nearly $60 M_{\oplus}$.⁶ In the case of planet c (Fig. 12, green curve), we find a much more controlled mass-loss process, reaching a starting point of about $17 M_{\oplus}$. This, and the fact that the future evolution of the atmosphere is stable against evaporation in the long run, makes the Earth-like core with 2 per cent atmosphere case plausible.

While it is possible to trace the planets further back in time, we stop at 0.5 Gyr since the results beyond that would be subjected to the further uncertainty associated with the stellar rotation rate during the saturation phase early in the star’s life.

Due to the uncertainty in the stellar age, we decided to test the same cases as before but with lower age values. We chose ages of 2.5, 4.5, and 6.5 Gyr and reran the models for both planets (Fig. 13).

⁶The hydrodynamic-based approximation works in the 1–39 M_{\oplus} mass range, so beyond this limit we use the energy limited approximation by Erkaev et al. (2007) to model the mass-loss.

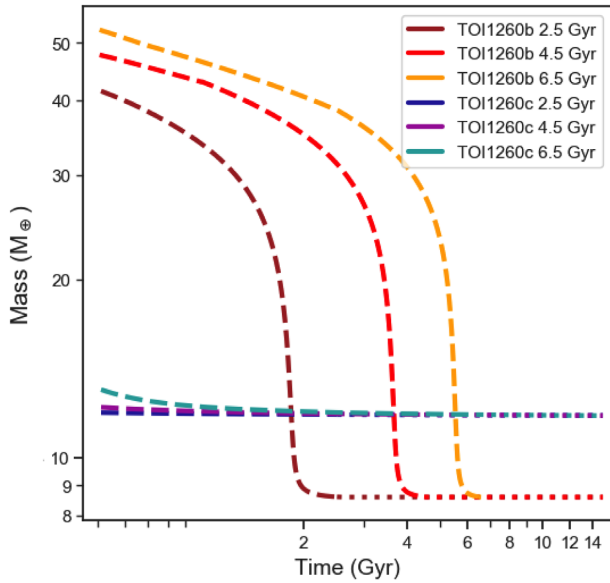


Figure 13. Mass temporal evolution of the TOI-1260 planets as per Fig. 12 but considering different stellar ages.

In short, we find that planet b still loses its atmosphere in about the same time frame (~ 100 Myr); planet c retains a long-term stable atmosphere as before and its temporal evolution is almost completely independent of the age of the star. This result is not so surprising when we consider the fact that the X-ray luminosity is most intense in the early evolutionary stages, during which most of the atmospheric mass-loss occurs. These results are generally consistent with the above findings for the nominal age, showing that the mass and radius evolution of the planets is robust for a wide range of stellar ages.

We, however, note, that 100 Myr is a short time compared to the overall life of the star, especially if the star is older. This makes it relatively unlikely that we would currently be witnessing the process of planet b losing a primary H-He atmosphere.

The fact that the nominal age is at the upper limit of the thin disc population age range (see Section 3.4), as well as the result that the mass evolution of both planets is well consistent with a significantly younger star, suggests the possibility that this star is, in fact, younger, which in turn emphasizes the fact that a high precision of the stellar age estimate can decrease the degeneracy in the determination of planet interiors.

5.2.3 Planetary composition and atmospheric characterization potential

Looking back to the two scenarios for TOI-1260b, we consider the composition of a 50 percent Earth-like core and 50 percent water-ice case, likely mixed rather than layered as suggested by Vazan, Sari & Kessel (2020), to be more probable. However, the above models do not take into account planet migration or rather assume orbit migration took place quickly (a few Myr) early in the system’s history, so a complex migration history could have played a role in this relatively old system. We also note that the X-ray luminosity evolution is calculated using a scaling law just for the mean value (Penz et al. 2008b) and does not account for different levels of high-energy radiation to which planets could be subjected during their early evolutionary stages. The effects of stellar wind and magnetically driven cataclysmic events originating from the stellar surface, which could affect the rate of photoevaporation, are also ignored. Furthermore, our simulations only consider the case

of H-He primary atmospheres. Thus, our results do not exclude the possibility of secondary envelopes, or primary envelopes of a different composition, which may in turn be smaller and more difficult to lose under atmospheric escape processes. The latter case could mean that TOI-1260b and TOI-1260c are representatives of a high-metallicity population of hot Neptunes as discussed in depth by Moses et al. (2013). Hu, Seager & Yung (2015) proposed the existence of He atmosphere planets, and that many sub-Neptune-sized exoplanets in short orbits could possess such atmospheres. They proposed that such an atmosphere could explain for example the emission and transmission spectra of GJ436b. While much smaller and less massive than GJ436b, TOI-1260b has a similar orbital period and equilibrium temperature, and could be a firm candidate to possess a He atmosphere. Those atmospheres contain trace amounts of hydrogen, carbon, and oxygen, with the predominance of CO over CH₄ as the main form of carbon (Hu et al. 2015), which could fit with the overall bulk composition of the planet determined here.

Another seemingly probable scenario, considering the planets’ proximity to the star and the implied intense insolation, coupled with an assumed high water content of both planets, could be that the observed radii are highly inflated as the atmospheres may be well-represented by supercritical hydrospheres (Mousis et al. 2020). Unfortunately, the transmission spectroscopy metrics (TSM; Kempton et al. 2018) for TOI-1260b and TOI-1260c are 44 and 42, respectively. This places both planets below the recommended TSM cutoff for planets with radii above $1.5 R_{\oplus}$ (TSM > 90). Still, ground-based high-resolution spectroscopy could probe for the presence of ongoing escape processes by observing the H α lines (Yan & Henning 2018) in the near-IR, as the Ly α line will be too absorbed by the interstellar medium at the system’s distance (~ 74 pc).

6 CONCLUSIONS

In this paper, we present the detection and characterization of the TOI-1260 system observed by *TESS* in Sectors 14 and 21. This K6 V star hosts two mini-Neptunes in short-period orbits confirmed by HARPS-N radial velocities, as well as a tentative outer planet, which is seen transiting in the *TESS* photometry in Sector 21.

We use GP regression to disentangle the stellar from the planet signals contained in our radial velocities. GPs offer a lot of flexibility, which may lead to the removal of genuine signals of planetary origin – a risk we mitigate by using the information provided by activity indicators, i.e. the relatively novel multidimensional GP approach.

We note, however, that in order to improve the mass characterization of the planets we need a strategic RV follow-up. More specifically, taking several observations within a single stellar rotation period, instead of sporadic observations, is a better strategy to disentangle stellar activity using GPs, since the latter rely on the correlation between points.

We perform simulations to evaluate the possibility of hydrodynamic atmospheric mass-loss, which demonstrated the difficulty in constraining the structure and composition of planets in $2-3 R_{\oplus}$ radius range. Our discussion thus emphasizes the fact that solely from the mass and radius we cannot distinguish between a planet being H₂O-dominated or a rocky planet with a significant envelope. Another constraint to our insight into similar systems is the large uncertainty on the systems’ ages. This could be remedied from a large sample of planet systems with well-determined ages, such as is attempted to be achieved by the core sample of the PLATO mission (Rauer et al. 2014), with projected uncertainties in its age determinations to be within 10 percent. In this paper, we further demonstrate the need to study close-in planets around low-mass stars to help constrain composition models and mass-loss mechanisms.

We add that the precision to which planetary masses are measured today is often insufficient to accomplish this to a satisfactory level, complicating our overall understanding of exoplanet demographics.

ACKNOWLEDGEMENTS

This work is done under the framework of the KESPRINT collaboration (<http://kesprint.science>). KESPRINT is an international consortium devoted to the characterization and research of exoplanets discovered with space-based missions.

IYG, CMP, MF, and JK gratefully acknowledge the support of the Swedish National Space Agency (DNR 174/18, 65/19, 2020-00104).

KWFM and ME acknowledge the support of the German Research Foundation (DFG) priority program SPP 1992 ‘Exploring the Diversity of Extrasolar Planets’ (RA714/14-1, HA3279/12-1).

HD acknowledges support from the Spanish Research Agency of the Ministry of Science and Innovation (AEI-MICINN) under grant PID2019-107061GB-C66, DOI: 10.13039/501100011033.

This work was supported by the Thüringer Ministerium für Wirtschaft, Wissenschaft und Digitale Gesellschaft.

This research has made use of the Exoplanet Follow-up Observation Program website, which is operated by the California Institute of Technology, under contract with the National Aeronautics and Space Administration under the Exoplanet Exploration Program.

This work makes use of observations from the LCOGT network.

Some of the Observations in the paper made use of the High-Resolution Imaging instrument ‘Alopec’. ‘Alopec’ was funded by the NASA Exoplanet Exploration Program and built at the NASA Ames Research Center by Steve B. Howell, Nic Scott, Elliott P. Horch, and Emmett Quigley. ‘Alopec’ is mounted on the Gemini North telescope of the international Gemini Observatory, a program of NOIRLab, which is managed by the Association of Universities for Research in Astronomy (AURA) under a cooperative agreement with the National Science Foundation. on behalf of the Gemini partnership: the National Science Foundation (United States), National Research Council (Canada), Agencia Nacional de Investigación y Desarrollo (Chile), Ministerio de Ciencia, Tecnología e Innovación (Argentina), Ministério da Ciência, Tecnologia, Inovações e Comunicações (Brazil), and Korea Astronomy and Space Science Institute (Republic of Korea).

This paper includes data collected by the *TESS* mission. Funding for the *TESS* mission is provided by the NASA Explorer Program. We acknowledge the use of public TOI Release data from pipelines at the *TESS* Science Office and at the *TESS* Science Processing Operations Center. Resources supporting this work were provided by the NASA High-End Computing (HEC) Program through the NASA Advanced Supercomputing (NAS) Division at Ames Research Center for the production of the SPOC data products. This research has made use of the Exoplanet Follow-up Observation Program website, which is operated by the California Institute of Technology, under contract with the National Aeronautics and Space Administration under the Exoplanet Exploration Program.

This work has made use of data from the European Space Agency (ESA) mission *Gaia* (<https://www.cosmos.esa.int/gaia>), processed by the *Gaia* Data Processing and Analysis Consortium (DPAC, <https://www.cosmos.esa.int/web/gaia/dpac/consortium>). Funding for the DPAC has been provided by national institutions, in particular the institutions participating in the *Gaia* Multilateral Agreement.

This research has made use of the VizieR catalogue access tool, CDS, Strasbourg, France (DOI: 10.26093/cds/vizier). The original description of the VizieR service was published in Ochsenbein, Bauer & Marcout (2000).

Based on observations made with the Italian Telescopio Nazionale Galileo (TNG) operated on the island of La Palma by the Fundación Galileo Galilei of the INAF (Istituto Nazionale di Astrofisica) at the Spanish Observatorio del Roque de los Muchachos of the Instituto de Astrofísica de Canarias under programmes CAT19A.162, ITP19.1 and A41TAC.49.

Facility: *TESS*, *Gaia*, TNG/HARPS-N, LCOGT.

Software: EXOTRANS, lightcurve, citlalicue, george, pytransit, IRAF, PARAM 1.5, SME, SpecMatch-emp, AstroImageJ, pyaneti, juliet, pyTTV.

DATA AVAILABILITY

The data underlying this article are available in the article and in its online supplementary material, as well as ExoFOP-TESS.⁷

REFERENCES

- Ambikasaran S., Foreman-Mackey D., Greengard L., Hogg D. W., O’Neil M., 2016, *IEEE Trans. Pattern Anal. Mach. Intell.*, 38, 252
- Baglin A. et al., 2006, 36th COSPAR Scientific Assembly, 3749
- Baranne A. et al., 1996, *A&AS*, 119, 373
- Barragán O. et al., 2019b, *MNRAS*, 490, 698
- Barragán O., Gandolfi D., Antoniciello G., 2019a, *MNRAS*, 482, 1017
- Berger T. A., Huber D., Gaidos E., van Saders J. L., Weiss L. M., 2020, *AJ*, 160, 108
- Borucki W. J. et al., 2010, *Science*, 327, 977
- Boyajian T. S. et al., 2012, *ApJ*, 757, 112
- Bressan A., Marigo P., Girardi L., Salasnich B., Dal Cero C., Rubele S., Nanni A., 2012, *MNRAS*, 427, 127
- Brown T. M. et al., 2013, *PASP*, 125, 1031
- Buchner J. et al., 2014, *A&A*, 564, A125
- Chambers J. E., 1999, *MNRAS*, 304, 793
- Choi J., Dotter A., Conroy C., Cantiello M., Paxton B., Johnson B. D., 2016, *ApJ*, 823, 102
- Ciardi D. R., Beichman C. A., Horch E. P., Howell S. B., 2015, *ApJ*, 805, 16
- Cloutier R., Menou K., 2020, *AJ*, 159, 211
- Collins K. A., Kielkopf J. F., Stassun K. G., Hessman F. V., 2017, *AJ*, 153, 77
- Cosentino R. et al., 2012, in Ian S. McLean, Suzanne K. Ramsay, Hideki Takami, eds, Proc SPIE Conf. Ser. Vol. 8446, Ground-based and Airborne Instrumentation for Astronomy IV. SPIE, Bellingham, p. 84461V
- Cosentino R. et al., 2014, in Johnson R. B., Mahajan V. N., Thibault N., eds, Proc. SPIE Conf. Ser. Vol. 91478, Ground-based and Airborne Instrumentation for Astronomy V. SPIE, Bellingham, p. 91478C
- Curtis J. L. et al., 2020, *ApJ*, 904, 140
- da Silva L. et al., 2006, *A&A*, 458, 609
- del Peloso E. F., da Silva L., Porto de Mello G. F., Arany-Prado L. I., 2005, *A&A*, 440, 1153
- Dong S., Xie J.-W., Zhou J.-L., Zheng Z., Luo A., 2018, *PNAS*, 115, 266
- Erkaev N. V., Kulikov Y. N., Lammer H., Selsis F., Langmayr D., Jaritz G. F., Biernat H. K., 2007, *A&A*, 472, 329
- Espinoza N., Kossakowski D., Brahm R., 2019, *MNRAS*, 490, 2262
- Foreman-Mackey D., Agol E., Ambikasaran S., Angus R., 2017, *Astrophysics Source Code Library*, record ascl:1709.008
- Foreman-Mackey D., Hoyer S., Bernhard J., Angus R., 2014, *george: George* (v0.2.0)
- Fridlund M. et al., 2017, *A&A*, 604, A16
- Fulton B. J. et al., 2017, *AJ*, 154, 109
- Fulton B. J., Petigura E. A., 2018, *AJ*, 156, 264
- Fulton B. J., Petigura E. A., Blunt S., Sinukoff E., 2018, *PASP*, 130, 044504
- Gaia Collaboration et al., 2021, *A&A*, 649, A6

⁷<https://exofof.ipac.caltech.edu/teess>

- Gregory P. C., 2005, *ApJ*, 631, 1198
- Grziwa S., Pätzold M., Carone L., 2012, *MNRAS*, 420, 1045
- Günther M. N. et al., 2019, *Nat. Astron.*, 3, 1099
- Gustafsson B., Edvardsson B., Eriksson K., Jørgensen U. G., Nordlund Å., Plez B., 2008, *A&A*, 486, 951
- Hirano T. et al., 2018, *AJ*, 155, 127
- Hodapp K. W. et al., 2003, *PASP*, 115, 1388
- Houdebine E. R., Mullan D. J., Bercu B., Paletou F., Gebran M., 2017, *ApJ*, 837, 96
- Howell S. B. et al., 2014, *PASP*, 126, 398
- Howell S. B., Everett M. E., Sherry W., Horch E., Ciardi D. R., 2011, *AJ*, 142, 19
- Hu R., Seager S., Yung Y. L., 2015, *ApJ*, 807, 8
- Jenkins J. M. et al., 2010, in Radziwill N. M., Bridger A., eds, Proc. SPIE Conf. Ser. Vol. 7740, Software and Cyberinfrastructure for Astronomy. SPIE, Bellingham, p. 77400D
- Jenkins J. M. et al., 2016, in Gianluca Chiozzi, Juan C. Guzman, eds, Proc. SPIE Conf. Ser. Vol. 9913, Software and Cyberinfrastructure for Astronomy IV. SPIE, Bellingham, p. 99133E
- Jenkins J. M., 2002, *ApJ*, 575, 493
- Jenkins J. M., Tenenbaum P., Seader S., Burke C. J., McCauliff S. D., Smith J. C., Twicken J. D., Chandrasekaran H., 2017, Kepler Data Processing Handbook: Transiting Planet Search. Kepler Science Document KSCI-19081-002
- Jensen E., 2013, Astrophysics Source Code Library, record ascl:1306.007
- Jurgenson C., Fischer D., McCracken T., Sawyer D., Szymkowiak A., Davis A., Muller G., Santoro F., 2016, in Evans C. J., Simard L., Takami H., eds, SPIE Conf. Ser. Vol. 9908, Ground-based and Airborne Instrumentation for Astronomy VI. SPIE, Bellingham, p. 99086T
- Kane S. R., 2015, *ApJ*, 814, L9
- Kane S. R., 2019, *AJ*, 158, 72
- Kempton E. M.-R. et al., 2018, *PASP*, 130, 114401
- Kipping D. M., 2013, *MNRAS*, 435, 2152
- Korth J., 2020, PhD thesis, Universität zu Köln, Available at: <https://kups.uni-koeln.de/11289/>
- Kostov V. B. et al., 2019, *AJ*, 158, 32
- Kovács G., Zucker S., Mazeh T., 2002, *A&A*, 391, 369
- Kreidberg L., 2015, *PASP*, 127, 1161
- Kubyskhina D. et al., 2018, *A&A*, 619, A151
- Kurucz R. L., 2013, Astrophysics Source Code Library, record ascl:1303.024
- Li G., Naoz S., Valsecchi F., Johnson J. A., Rasio F. A., 2014, *ApJ*, 794, 131
- Lightkurve Collaboration, 2018, Astrophysics Source Code Library, record ascl:1812.013
- Lissauer J. J. et al., 2011, *ApJS*, 197, 8
- Locci D., Cecchi-Pestellini C., Micela G., 2019, *A&A*, 624, A101
- Lopez E. D., Fortney J. J., 2013, *ApJ*, 776, 2
- Lopez E. D., Fortney J. J., 2014, *ApJ*, 792, 1
- Luque R. et al., 2021, *A&A*, 645, A41
- Mamajek E. E., Hillenbrand L. A., 2008, *ApJ*, 687, 1264
- Mandel K., Agol E., 2002, *ApJ*, 580, L171
- Mayo A. W. et al., 2019, *AJ*, 158, 165
- Mayor M. et al., 2003, The Messenger, 114, 20
- McDonald G. D., Kreidberg L., Lopez E., 2019a, *ApJ*, 876, 22
- Morris R. L., Twicken J. D., Smith J. C., Clarke B. D., Jenkins J. M., Bryson S. T., Girouard F., Klaus T. C., 2017, Kepler Data Processing Handbook: Photometric Analysis. Kepler Science Document KSCI-19081-002
- Morton T. D., 2015, Astrophysics Source Code Library, record ascl:1503.010
- Moses J. I. et al., 2013, *ApJ*, 777, 34
- Mousis O., Deleuil M., Aguichine A., Marcq E., Naar J., Aguirre L. A., Brugger B., Gonçalves T., 2020, *ApJ*, 896, L22
- Ochsenbein F., Bauer P., Marcout J., 2000, *A&AS*, 143, 23
- Ofir A., 2014, *A&A*, 561, A138
- Osborn H. P. et al., 2016, *MNRAS*, 457, 2273
- Otegi J. F., Bouchy F., Helled R., 2020, *A&A*, 634, A43
- Owen J. E., Wu Y., 2013, *ApJ*, 775, 105
- Parviainen H., 2015, *MNRAS*, 450, 3233
- Penz T., Micela G., Lammer H., 2008a, *A&A*, 477, 309
- Penz T., Micela G., Lammer H., 2008b, *A&A*, 477, 309
- Pepe F. A. et al., 2010, in McLean I. S., Ramsay S. K., Takami H., eds, SPIE Conf. Ser. Vol. 7735, Ground-based and Airborne Instrumentation for Astronomy III. SPIE, Bellingham, p. 77350F
- Pepe F. et al., 2021, *A&A*, 645, A96
- Persson C. M. et al., 2018, *A&A*, 618, A33
- Piskunov N., Valenti J. A., 2017, *A&A*, 597, A16
- Poppenhaeger K., Ketzler L., Mallonn M., 2021, *MNRAS*, 500, 4560
- Quirrenbach A. et al., 2014, in Ramsay S. K., McLean I. S., Takami H., eds, SPIE Conf. Ser. Vol. 9147, Ground-based and Airborne Instrumentation for Astronomy V. SPIE, Bellingham, p. 91471F
- Quirrenbach A. et al., 2018, in Evans C. J., Simard L., Takami H., eds, Proc. SPIE Conf. Ser. Vol. 10702, Ground-based and Airborne Instrumentation for Astronomy VII. SPIE, Bellingham, p. 107020W
- Rajpaul V., Aigrain S., Osborne M. A., Reece S., Roberts S., 2015, *MNRAS*, 452, 2269
- Rauer H. et al., 2014, *Exp. Astron.*, 38, 249
- Reddy B. E., Lambert D. L., Allende Prieto C., 2006, *MNRAS*, 367, 1329
- Ricker G. R. et al., 2015, *J. Astron. Telesc. Instrum. Syst.*, 1, 014003
- Rodriguez J. E. et al., 2019, *AJ*, 157, 191
- Ryabchikova T., Piskunov N., Kurucz R. L., Stempels H. C., Heiter U., Pakhomov Y., Barklem P. S., 2015, *Phys. Scr.*, 90, 054005
- Sanz-Forcada J., Micela G., Ribas I., Pollock A. M. T., Eiroa C., Velasco A., Solano E., García-Álvarez D., 2011, *A&A*, 532, A6
- Schlegel D. J., Finkbeiner D. P., Davis M., 1998, *ApJ*, 500, 525
- Smith J. C. et al., 2012, *PASP*, 124, 1000
- Southworth J., Wheatley P. J., Sams G., 2007, *MNRAS*, 379, L11
- Speagle J. S., 2020, *MNRAS*, 493, 3132
- Stassun K. G. et al., 2018b, *AJ*, 156, 102
- Stassun K. G., Collins K. A., Gaudi B. S., 2017, *AJ*, 153, 136
- Stassun K. G., Corsaro E., Pepper J. A., Gaudi B. S., 2018a, *AJ*, 155, 22
- Stassun K. G., Kratter K. M., Scholz A., Dupuy T. J., 2012, *ApJ*, 756, 47
- Stassun K. G., Torres G., 2016, *AJ*, 152, 180
- Stassun K. G., Torres G., 2018, *ApJ*, 862, 61
- Stumpe M. C. et al., 2012, *PASP*, 124, 985
- Suárez Mascareño A., Rebolo R., González Hernández J. I., Esposito M., 2015, *MNRAS*, 452, 2745
- Suárez Mascareño A., Rebolo R., González Hernández J. I., Esposito M., 2016, *MNRAS*, 457, 2604
- Torres G., 2010, *AJ*, 140, 1158
- Twicken J. D. et al., 2018, *PASP*, 130, 064502
- Twicken J. D., Clarke B. D., Bryson S. T., Tenenbaum P., Wu H., Jenkins J. M., Girouard F., Klaus T. C., 2010, in Radziwill N. M., Bridger A., eds, Proc. SPIE Conf. Ser. Vol. 7740, Software and Cyberinfrastructure for Astronomy. SPIE, Bellingham, p. 774023
- Valencia D., Sasselov D. D., O'Connell R. J., 2007, *ApJ*, 665, 1413
- Valenti J. A., Piskunov N., 1996, *A&AS*, 118, 595
- Van Eylen V. et al., 2019, *AJ*, 157, 61
- Van Eylen V. et al., 2021, preprint([arXiv:2101.01593](https://arxiv.org/abs/2101.01593))
- Van Eylen V., Agentoft C., Lundkvist M. S., Kjeldsen H., Owen J. E., Fulton B. J., Petigura E., Snellen I., 2018, *MNRAS*, 479, 4786
- Vazan A., Sari R., Kessel R., 2020, preprint([arXiv:2011.00602](https://arxiv.org/abs/2011.00602))
- Vogt S. S. et al., 1994, in Crawford D. L., Craine E. R., eds, SPIE Conf. Ser. Vol. 2198, Instrumentation in Astronomy VIII. SPIE, Bellingham, p. 362
- Wilson R. F. et al., 2018, *AJ*, 155, 68
- Wu Y., 2019, *ApJ*, 874, 91
- Yan F., Henning T., 2018, *Nat. Astron.*, 2, 714
- Yee S. W., Petigura E. A., von Braun K., 2017, *ApJ*, 836, 77
- Zechmeister M. et al., 2018, *A&A*, 609, A12
- Zechmeister M., Kürster M., 2009, *A&A*, 496, 577
- Zeng L. et al., 2019, *Proc. Natl. Acad. Sci.*, 116, 9723
- Zeng L., Sasselov D. D., Jacobsen S. B., 2016, *ApJ*, 819, 127

APPENDIX A: HARPS-N DATA

Table A1. Radial velocities and spectral activity indicators measured from TNG/HARPS-N spectra.

BJD _{TDB} (d) -2457000	RV (m s ⁻¹)	σ_{RV} (m s ⁻¹)	CRX (m s ⁻¹ Np ⁻¹)	σ_{CRX} (m s ⁻¹ Np ⁻¹)	dW (m ² s ⁻²)	σ_{dW} (m ² s ⁻²)	H α	$\sigma_{H\alpha}$	NaD ₁	σ_{NaD_1}	NaD ₂	σ_{NaD_2}	BIS (m s ⁻¹)	σ_{BIS} (m s ⁻¹)	CCF_FHWM (km s ⁻¹)	CCF_CTR	S-index	$\sigma_{S-index}$	SNR	T_{exp} (s)
1862.62923	6.677	1.716	-17.725	14.096	-2.805	3.196	0.6841	0.0020	0.2004	0.0024	0.2252	0.0026	40.628	3.763	6.364	42.479	1.133	0.025	38.7	3600.0
1862.66579	4.803	1.340	-9.964	11.112	-7.302	2.351	0.6850	0.0017	0.1974	0.0020	0.2216	0.0021	50.620	3.022	6.361	42.637	1.122	0.019	45.9	3600.0
1863.67080	10.163	1.235	10.432	10.103	-17.998	1.895	0.6832	0.0013	0.1945	0.0014	0.2200	0.0015	47.085	2.120	6.360	42.878	1.134	0.012	61.2	3600.0
1863.78184	11.454	1.180	10.563	9.470	-15.791	1.870	0.6844	0.0012	0.1951	0.0014	0.2196	0.0015	52.086	2.173	6.363	42.821	1.135	0.012	59.9	3600.0
1864.64888	15.901	1.490	14.765	12.360	-3.886	2.166	0.6855	0.0018	0.1975	0.0020	0.2236	0.0022	56.202	3.091	6.371	42.728	1.154	0.021	45.1	3600.0
1864.76150	13.179	1.573	20.240	13.193	-6.655	2.239	0.6827	0.0019	0.1968	0.0021	0.2284	0.0023	46.279	3.192	6.363	42.705	1.168	0.022	44.2	3600.0
1865.63156	5.489	1.193	14.321	10.311	-8.966	2.404	0.6816	0.0017	0.1991	0.0016	0.2245	0.0018	49.886	2.354	6.380	42.741	1.141	0.014	56.3	3600.0
1865.76718	1.903	1.434	19.806	11.892	-8.575	2.433	0.6913	0.0016	0.2000	0.0016	0.2219	0.0018	47.921	2.470	6.381	42.767	1.169	0.016	54.5	3600.0
1869.71163	0.562	1.555	-9.033	12.511	-1.288	2.907	0.6875	0.0017	0.2007	0.0021	0.2282	0.0023	63.711	3.314	6.383	42.718	1.193	0.022	41.9	3600.0
1896.56585	15.450	1.436	-3.060	11.637	-1.510	2.297	0.6878	0.0016	0.2237	0.0020	0.2459	0.0021	45.665	2.994	6.384	42.720	1.214	0.019	45.9	3600.0
1896.67552	13.918	1.388	-11.290	11.143	-0.808	2.814	0.6945	0.0016	0.2284	0.0020	0.2467	0.0022	43.192	3.018	6.386	42.659	1.232	0.019	45.8	3600.0
1898.56841	7.774	1.073	-3.532	8.928	0.857	2.620	0.7382	0.0014	0.2165	0.0015	0.2407	0.0016	56.588	2.184	6.387	42.631	1.446	0.013	60.1	3600.0
1925.63670	17.927	1.749	-2.160	14.638	-1.086	3.147	0.6863	0.0023	0.2479	0.0030	0.2599	0.0032	43.613	4.335	6.393	42.655	1.123	0.032	34.8	3600.0
1926.64886	19.622	2.118	-15.619	17.407	0.278	2.686	0.7005	0.0019	0.2343	0.0025	0.2600	0.0027	61.432	3.705	6.379	42.775	1.199	0.026	39.4	3300.0
1929.63674	10.128	1.193	-1.733	10.068	-7.456	2.374	0.6858	0.0018	0.2118	0.0020	0.2432	0.0022	64.774	2.971	6.372	42.772	1.175	0.020	47.1	3006.7
1930.42198	11.743	2.290	-24.218	19.108	-6.858	3.472	0.6937	0.0028	0.2339	0.0036	0.2459	0.0039	72.455	5.391	6.359	42.761	1.026	0.054	29.6	2200.0
1969.53394	-0.344	2.607	30.922	21.458	-23.205	3.971	0.6870	0.0031	0.3179	0.0047	0.3119	0.0049	52.253	6.453	6.339	42.808	1.146	0.041	25.9	3600.0
1971.52051	-2.375	1.298	-6.884	10.783	-44.328	2.698	0.6768	0.0016	0.2088	0.0019	0.2320	0.0021	63.058	2.849	6.316	43.145	1.011	0.019	48.1	3600.0
2000.41367	2.216	1.268	-8.945	10.158	-36.375	2.377	0.6827	0.0014	0.2021	0.0017	0.2323	0.0019	70.680	2.731	6.333	43.037	1.098	0.018	48.8	3600.0
2000.45426	4.378	1.489	-35.801	10.971	-25.136	2.493	0.6822	0.0015	0.2101	0.0021	0.2300	0.0022	75.663	3.223	6.333	43.001	1.067	0.022	42.4	3600.0
2001.42014	0.440	1.116	-11.500	8.915	-47.568	1.854	0.6692	0.0011	0.1937	0.0012	0.2238	0.0014	63.516	1.940	6.312	43.220	1.038	0.010	65.8	3600.0
2001.46039	-0.236	0.949	-23.011	7.095	-48.208	1.735	0.6705	0.0010	0.1916	0.0011	0.2242	0.0012	73.278	1.702	6.312	43.235	1.024	0.009	73.8	3600.0
2002.42024	-2.632	0.905	5.811	7.749	-53.132	2.055	0.6726	0.0014	0.1975	0.0014	0.2341	0.0016	56.605	1.996	6.303	43.312	1.001	0.011	64.2	3600.0
2002.46195	-0.506	1.311	13.103	10.881	-55.646	2.419	0.6712	0.0013	0.1967	0.0014	0.2353	0.0015	63.482	1.999	6.302	43.323	1.024	0.011	64.4	3600.0
2011.40922	27.029	2.205	-0.278	18.301	-29.220	3.238	0.6777	0.0024	0.1989	0.0033	0.2373	0.0036	48.672	5.219	6.321	43.031	1.123	0.041	30.2	3300.0
2011.44218	23.398	2.840	16.880	23.534	-	4.204	0.6794	0.0034	0.2268	0.0054	0.2724	0.0060	8.605	8.605	6.334	42.874	1.069	0.075	20.8	2999.1
2012.40959	25.530	1.828	20.100	17.729	-24.200	2.180	0.6723	0.0016	0.2009	0.0020	0.2305	0.0022	33.998	3.095	6.349	42.922	1.105	0.021	45.2	3300.0
2012.44888	25.937	1.907	13.461	15.545	-27.838	2.505	0.6822	0.0018	0.2038	0.0022	0.2337	0.0024	45.139	3.518	6.342	42.933	1.157	0.026	40.7	3300.0
2013.42280	17.344	1.733	30.803	13.985	-20.223	2.502	0.6878	0.0020	0.2484	0.0025	0.2671	0.0026	35.178	3.499	6.354	42.858	1.152	0.024	41.5	3300.0
2013.44892	17.566	2.332	0.142	20.049	-13.318	4.085	0.6896	0.0035	0.2526	0.0049	0.2816	0.0054	54.908	7.476	6.371	42.777	1.121	0.063	23.7	1353.0
2013.47580	26.451	3.139	39.435	26.754	-9.109	5.318	0.6887	0.0042	0.3239	0.0064	0.3563	0.0069	14.612	8.586	6.351	42.772	1.103	0.075	21.0	2273.7
2014.42732	30.021	1.846	-7.137	15.000	-13.315	2.384	0.6837	0.0017	0.2265	0.0024	0.2527	0.0025	46.902	3.644	6.370	42.766	1.168	0.027	39.5	3300.0
2014.46531	28.500	1.704	16.941	13.691	-14.391	3.104	0.6796	0.0018	0.2181	0.0024	0.2506	0.0026	39.564	3.733	6.360	42.848	1.165	0.029	39.0	3300.0

APPENDIX B: MONOTRANSIT PERIODS

Table B1. Possible periods and period ranges for the case of a unique single transit assuming a circular orbit. The excluded values/gaps correspond to transit times when a transit event would be seen in the light curves. The calculations were performed in steps of 0.1 d and include the data gap in Sector 14 as a possible location of a missed transit. The table does not include the 16.6-d period corresponding to the scenario of overlapping transits of this tentative planet and planet c, described in the text. If this period is correct, this would imply the presence of two transits in Sector 21.

Period (d)
20.3
22.8
26.0–26.1
28.0–28.1
30.4
32.7–33.8
36.4–36.5
39.2–42.2
45.5–45.7
49.0–56.3

¹Department of Space, Earth and Environment, Chalmers University of Technology, Onsala Space Observatory, SW-439 92 Onsala, Sweden

²Sub-department of Astrophysics, Department of Physics, University of Oxford, Oxford OX1 3RH, UK

³Instituto de Astrofísica de Canarias, 38205 La Laguna, Tenerife, Spain

⁴Departamento de Astrofísica, Universidad de La Laguna, 38206 La Laguna, Tenerife, Spain

⁵Leiden Observatory, Leiden University, 2333 CA, Leiden, the Netherlands

⁶INAF – Osservatorio Astronomico di Palermo, Piazza del Parlamento 1, I-90134 Palermo, Italy

⁷Astronomy Department and Van Vleck Observatory, Wesleyan University, Middletown, CT 06459, USA

⁸Dipartimento di Fisica, Università di Torino, via P. Giuria 1, I-10125 Torino, Italy

⁹Department of Earth and Planetary Sciences, University of California, Riverside, CA 92521, USA

¹⁰Department of Space, Earth and Environment, Astronomy and Plasma Physics, Chalmers University of Technology, SE-412 96 Gothenburg, Sweden

¹¹Vanderbilt University, Physics and Astronomy Department, Nashville, TN 37235, USA

¹²Department of Astronomy, University of Tokyo, 7-3-1 Hongo, Bunkyo-ku, Tokyo 113-0033, Japan

¹³Department of Physics and Kavli Institute for Astrophysics and Space Research, Massachusetts Institute of Technology, Cambridge, MA 02139, USA

¹⁴Observatoire de l'Université de Genève, Chemin des Maillettes 51, CH-1290 Versoix, Switzerland

¹⁵Center for Astrophysics | Harvard & Smithsonian, 60 Garden Street, Cambridge, MA 02138, USA

¹⁶NASA Ames Research Center, Moffett Field, CA 94035, USA

¹⁷Stellar Astrophysics Centre, Department of Physics and Astronomy, Aarhus University, Ny Munkegade 120, DK-8000 Aarhus C, Denmark

¹⁸Nordic Optical Telescope, Apartado 474, E-38700 Santa Cruz de La Palma, Santa Cruz de Tenerife, Spain

¹⁹Space Telescope Science Institute, 3700 San Martin Dr, Baltimore, MD 21218, USA

²⁰NASA Exoplanet Science Institute – Caltech/IPAC Pasadena, CA 91125 USA

²¹Center for Planetary Systems Habitability and McDonald Observatory, The University of Texas, Austin, TX 78712, USA

²²NASA Goddard Space Flight Center, Exoplanets and Stellar Astrophysics Laboratory (Code 667), Greenbelt, MD 20771, USA

²³Department of Physics and Astronomy, University of Kansas, Lawrence, KS 66045, USA

²⁴Institute of Planetary Research, German Aerospace Center (DLR), Rutherfordstraße 2, D-12489 Berlin, Germany

²⁵Thüringer Landessternwarte Tautenburg, Sternwarte 5, D-07778 Tautenburg, Germany

²⁶NASA Exoplanet Science Institute, Caltech/IPAC, Mail Code 100-22, 1200 E. California Blvd., Pasadena, CA 91125, USA

²⁷Department of Astronomy and Tsinghua Centre for Astrophysics, Tsinghua University, Beijing 100084, China

²⁸Department of Astronomy and Astrophysics, University of California, Santa Cruz, 1156 High St. Santa Cruz, CA 95064, USA

²⁹Rheinisches Institut für Umweltforschung an der Universität zu Köln, Aachener Strasse 209, E-50931 Köln, Spain

³⁰Observatori Astronòmic Albanyà, Camí de Bassegoda S/N, Albanyà, E-17733 Girona, Spain

³¹Astrobiology Center, NINS, 2-21-1 Osawa, Mitaka, Tokyo 181-8588, Japan

³²National Astronomical Observatory of Japan, NINS, 2-21-1 Osawa, Mitaka, Tokyo 181-8588, Japan

³³Department of Physics & Astronomy, Swarthmore College, Swarthmore, PA 19081, USA

³⁴Astronomical Institute ASCR, Fričova 298, CZ-251 65 Ondřejov, Czech Republic

³⁵Center for Astronomy and Astrophysics, Technical University Berlin, Hardenbergstr 36, D-10623 Berlin, Germany

³⁶U.S. Naval Observatory, Washington, DC 20392, USA

³⁷Proto-Logic LLC, 1718 Euclid Street NW, Washington, DC 20009, USA

³⁸Mullard Space Science Laboratory, University College London, Holmbury St Mary, Dorking, Surrey RH5 6NT, UK

³⁹NASA Goddard Space Flight Center, 8800 Greenbelt Road, Greenbelt, MD 20771, USA

⁴⁰Department of Earth, Atmospheric and Planetary Sciences, Massachusetts Institute of Technology, Cambridge, MA 02139, USA

⁴¹Department of Aeronautics and Astronautics, MIT, 77 Massachusetts Avenue, Cambridge, MA 02139, USA

⁴²SETI Institute, Mountain View, CA 94043, USA

⁴³Department of Astrophysical Sciences, Princeton University, 4 Ivy Lane, Princeton, NJ 08544, USA

This paper has been typeset from a \LaTeX file prepared by the author.